



EASTLAND PORT MAINTENANCE DREDGING AND DISPOSAL PROJECT

Hydrodynamic hindcast validation
Report prepared for Eastland Port

September 2017

MetOcean Solutions Ltd: Report P0331-04

September 2017

Report status

Version	Date	Status	Approved by
RevA	15/07/2017	Draft for internal review	Monetti
RevB	30/08/2017	Draft for internal review	Beamsley
RevC	11/09/2017	Draft for internal review	Monetti
RevD	21/09/2017	Draft for client review	Beamsley

It is the responsibility of the reader to verify the currency of the version number of this report.

The information, including the intellectual property, contained in this report is confidential and proprietary to MetOcean Solutions Ltd. It may be used by the persons to whom it is provided for the stated purpose for which it is provided, and must not be imparted to any third person without the prior written approval of MetOcean Solutions Ltd. MetOcean Solutions Ltd reserves all legal rights and remedies in relation to any infringement of its rights in respect of its confidential information.

TABLE OF CONTENTS

1.	Introduction	7
2.	Model methods.....	10
2.1.	Bathymetry.....	10
2.2.	ROMS model.....	11
2.3.	SCHISM model	11
2.4.	Modelling setup	12
2.4.1.	ROMS domain setup.....	12
2.4.2.	SCHISM domain setup.....	14
2.5.	Atmospheric forcing.....	16
2.6.	Tidal forcing.....	16
2.7.	Open boundary conditions.....	17
2.8.	River forcing.....	17
2.9.	ROMS model validation methods	21
2.9.1.	Definition of initial uncertainties	22
2.9.2.	Evaluation criteria	23
2.9.3.	Comparison between model and literature-described patterns.....	24
2.9.4.	Instrument deployment.....	24
2.10.	SCHISM model validation methods	26
3.	Results	27
3.1.	Qualitative validation	27
3.1.1.	Influence of shelf currents on the inner circulation.....	27
3.1.2.	Influence of river discharge on the inner circulation.....	29
3.1.3.	Mixing processes within Poverty bay.....	32
3.2.	Quantitative validation	36
3.2.1.	Wind climate	36
3.2.2.	ROMS water elevation and current velocities.....	40
3.2.1.	SCHISM water elevation and current velocities.....	51
4.	Summary.....	55
5.	References.....	56
	Appendix A. Measured and hindcast Wind Roses at Hicks Bay.....	57
	Appendix B. Monthly depth-averaged and surface current fields	58

LIST OF FIGURES

Figure 1.1 Maps showing the location of Poverty Bay (a and b), and Eastland Port (c) with the locations used in the present study. Both offshore disposal and shipping channel are indicated on top of the bathymetry in (d). 8

Figure 1.2 Flow chart showing the numerical modelling process for the study. Red lines indicate hydrodynamics; blue indicate waves; green indicate wind; brown indicate bathymetry; and yellow lines indicate sediments..... 9

Figure 2.1 Map showing both the 500 x 500 m (top) and the 5 x 5 m (bottom) gridded bathymetries used to interpolate the water depth to the computational grid in ROMS and SCHISM. 10

Figure 2.2 Map showing the downscaling approach used to adequately transfer the energy gradually from larger to smaller scales. Yellow rectangles indicate the ROMS domains implemented in the numerical modelling process. NZ, Gisborne and Poverty Bay ROMS grids are characterised by 8 km, 1 km and 150 m resolutions, respectively. Details specific to each set-up are presented in Table 2.1. 13

Figure 2.3 Unstructured mesh-grid used in SCHISM to simulate the hydrodynamics over Poverty Bay (left) and Eastland Port (right) 14

Figure 2.4 Model bathymetries (below mean sea level) over Poverty Bay (left) and Eastland Port (right). 15

Figure 2.5 Section from the port entrance, and along the navigation channel showing the LSC2 grid used in this study. 16

Figure 2.6 Time series of 3-hourly river discharges within Poverty Bay between 1990 and 2016. (a) locations where river discharge and water elevation data were collected by NIWA, (b) Waipaoa river discharge at Matawhero used in the ROMS model and (c) sum of the Waimata and Taruheru river discharge data used in the ROMS model. Data gaps in the measured time series were filled using monthly climatological averages..... 18

Figure 2.7 Map showing the regional bathymetry of the continental shelf between Gisborne and East Cape. The white dots indicate the sites used to compare hindcast and weather station wind data. 23

Figure 2.8 Map showing the bathymetry over the Gisborne continental shelf (a) and Poverty Bay (b). The red dots indicate the sites used to validate the ROMS hydrodynamic model against ADCP and S4 current meter data recorded in 1996, 1998 and 2010 (R.P. Hale, Old Dominion University; A.S. Ogston, University of Washington, School of Oceanography)..... 26

Figure 3.1 Daily depth-averaged current fields predicted by ROMS for March 2nd 1999 within Poverty Bay and over the adjacent continental shelf region. 28

Figure 3.2 Daily depth-averaged current fields predicted by ROMS for March 10th 1999 within Poverty Bay and over the adjacent continental shelf region. 28

Figure 3.3 Monthly depth-averaged (a) and surface (b) current fields predicted by ROMS for March 1999 within Poverty Bay and over the adjacent continental shelf region..... 30

Figure 3.4 Monthly depth-averaged (a) and surface (b) current fields predicted by ROMS for July 1999 within Poverty Bay and over the adjacent continental shelf region..... 31

Figure 3.5	Monthly surface (top) and 5 m (bottom) salinity predicted by ROMS for February 1999 within Poverty Bay and over the adjacent continental shelf region.....	33
Figure 3.6	Monthly surface (top) and 5 m (bottom) salinity predicted by ROMS for February 1999 within Poverty Bay and over the adjacent continental shelf region.....	34
Figure 3.7	Average flow pattern under NW winds influence at Poverty Bay: (a) average surface currents predicted by ROMS during NW wind episodes; (b) average near-bed currents predicted by ROMS during NW wind episodes; (c) position of the transect used to examine the spatial variations of the temperature in ROMS; (d) Average temperature section extracted from the ROMS outputs for NW wind episodes.....	35
Figure 3.8	Measured and modelled wind speed at 10 m between (a) June and December 2002, and (b) January and June 2003.....	37
Figure 3.9	Quantile-Quantile plot of the 10 m measured and model wind speeds at Gisborne Airport for the period 2000 – 2008.....	38
Figure 3.10	Measured (top) and model (bottom) wind roses at Gisborne Airport for the period 2000 – 2008. Winds are reported in the “coming from” directional reference.....	39
Figure 3.11	Comparison between measured and ROMS hindcast current and water elevation (c) time series at site DW at 11 m (a) and 31 m (b) (below sea level).....	41
Figure 3.12	Quantile-Quantile plots created from measured and ROMS hindcast current and water elevation (c) time series at site DW at 11 m (a) and 31 m (b) (below sea level). The dashed black line indicates a perfect agreement between the distributions.....	42
Figure 3.13	Comparison between measured and ROMS hindcast current time series at site NT at 18 m (a) and 35 m (b) (below sea level) for the second deployment.....	43
Figure 3.14	Quantile-Quantile plots created from measured and ROMS hindcast current time series at site N) at 18 m (a) and 35 m (b) (below sea level) for the second deployment. The dashed black line indicates a perfect agreement between the distributions.....	44
Figure 3.15	Comparison between measured and ROMS hindcast current time series at site N) at 18 m (a) and 35 m (b) (below sea level) for the third deployment.....	45
Figure 3.16	Quantile-Quantile plots created from measured and ROMS hindcast current time series at siteNT at 18 m (a) and 35 m (b) (below sea level) for the third deployment. The dashed black line indicates a perfect agreement between the distributions.....	46
Figure 3.17	Comparison between measured and ROMS hindcast current time series at site DT at 35 m (a) and 69 m (b) (below sea level) for the third deployment.....	47
Figure 3.18	Quantile-Quantile plots created from measured and ROMS hindcast current time series at site DT at 35 m (a) and 69 m (b) (below sea level) for the third deployment. The dashed black line indicates a perfect agreement between the distributions.....	48
Figure 3.19	Comparison between measured and ROMS hindcast current (a) and water elevation (b) time series at site CM2 at 10 m (below sea level) for the second deployment.....	49

Figure 3.20	Quantile-Quantile plot created from measured and ROMS hindcast current time series at site CM2 at 10 m (below sea level) for the second deployment. The dashed black line indicates a perfect agreement between the distributions.	50
Figure 3.21	Comparison between measured and ROMS hindcast current time series at site CM6 at 13 m (below sea level).....	50
Figure 3.22	Quantile-Quantile plot created from measured and ROMS hindcast current time series at site CM6 at 13 m (below sea level). The dashed black line indicates a perfect agreement between the distributions.	51
Figure 3.23	Comparison between measured and SCHISM hindcast current (a) and water elevation (b) time series at site CM2 at 10 m (below sea level) for the first and second deployment, respectively.	52
Figure 3.24	Quantile-Quantile plot created from measured and SCHISM hindcast current time series at site CM2 at 10 m (below sea level). The dashed black line indicates a perfect agreement between the distributions.	53
Figure 3.25	Comparison between measured and SCHISM hindcast current time series at site CM6 at 13 m (below sea level).....	53
Figure 3.26	Quantile-Quantile plot created from measured and SCHISM hindcast current time series at site CM6 at 13 m (below sea level). The dashed black line indicates a perfect agreement between the distributions.	54
Figure A.1	Measured and hindcast wind rose at 10 m extracted at Hicks Bay between 2000 and 2008.	57
Figure B.1	Monthly depth-averaged and surface current velocities for August (left) and September 1998 (right) predicted by ROMS.	58
Figure B.2	Monthly depth-averaged and surface current velocities for October (left) and November 1998 (right) predicted by ROMS.	59
Figure B.3	Monthly depth-averaged and surface current velocities for December (left) and January 1998/99 (right) predicted by ROMS.	60
Figure B.4	Monthly depth-averaged and surface current velocities for February (left) and March 1999 (right) predicted by ROMS.....	61
Figure B.5	Monthly depth-averaged and surface current velocities for April (left) and May 1999 (right) predicted by ROMS.....	62
Figure B.6	Monthly depth-averaged and surface current velocities for June (left) and July 1999 (right) predicted by ROMS.	63

LIST OF TABLES

Table 2.1	Relevant characteristics of ROMS domains.....	12
Table 2.2	Annual and monthly Turanganui river discharge statistics calculated from combined Waimata and Taruheru river discharges.....	19
Table 2.3	Monthly Waipaoa river discharge statistics at Matawhero.....	20
Table 2.4	Annual Waipaoa river discharge measured at Matawhero – Part 1.....	20
Table 2.5	Annual Waipaoa river discharge measured at Matawhero – Part 2.....	21
Table 2.6	Geographic coordinates, observational durations, samplings, record levels and water depths of the ADCP and S4 current meter deployments over Poverty Bay and the adjacent shelf margin.....	25
Table 3.1	Comparison of measured and hindcast wind data. Accuracy measures for wind speed at Gisborne Airport between 2000 and 2008.....	37
Table 3.2	Comparison between measured and ROMS hindcast hydrodynamic data. Accuracy measures for current speed and water elevation at several sites over Poverty Bay and the adjacent shelf margin.....	40
Table 3.3	Comparison between measured and SCHISM hindcast hydrodynamic data. Accuracy measures for current speed at two sites within Poverty Bay.....	51

1. INTRODUCTION

Eastland Port Ltd are seeking to renew their maintenance dredging and disposal consents at the Port of Gisborne.

Currently, dredged sediment is disposed at an offshore disposal site situated in approximately 18 – 20 m water depth (**Error! Reference source not found.**), with an average annual rate of approximately 73,000 m³ based on estimates obtained between 2002 and 2019 by Eastland Port.

Maintenance dredging is expected to occur using the Trailing Suction Hopper Dredge (TSHD) “Pukunui” although, if there are significant inflows of sediment due to large storm events, a higher productivity Trailing Suction Hopper Dredge (TSHD) may be required to ensure the required port and channel depths can be maintained. It is likely that some maintenance dredging may also be undertaken using a Backhoe Dredger (BHD) or Cutter Suction Dredger (CSD).

MetOcean Solutions (MOS) has been contracted to provide coastal oceanographic expertise to investigate both physical and morphological effects and associated sediment transport patterns resulting from the dredging and disposal of maintenance dredging material at the current disposal site.

For this purpose, a modelling approach has been developed which nest the Finite-element (FE) unstructured-grid SCHISM model within a coarser Regional Ocean Modelling System (ROMS) model to perform a dynamical downscaling of the circulation from deep ocean areas to the eastern shelf of the North Island (New Zealand) and Poverty Bay. At the regional scale, a 10-year ROMS hindcast is used to quantify the hydrodynamic climate of the shelf and Poverty Bay, inclusive of fluvial discharges. A 2-year, higher resolution FE hydrodynamic model (SCHISM) is used to quantify the detailed hydrodynamics within the bay (see flow chart in Figure 1.2). Calibration and validation of the hydrodynamic models was performed using *in situ* measured data recorded in Poverty Bay and the adjacent shelf margin.

The applied methodology is provided in Section 2, including a description of the model domains and configuration, forcing and boundary conditions, calibration and validation methods, and available measured datasets. Results of the calibration and validation processes are provided and discussed in Section 3. A brief summary is presented in Section 4 while the references cited in this document are listed in Section 5.

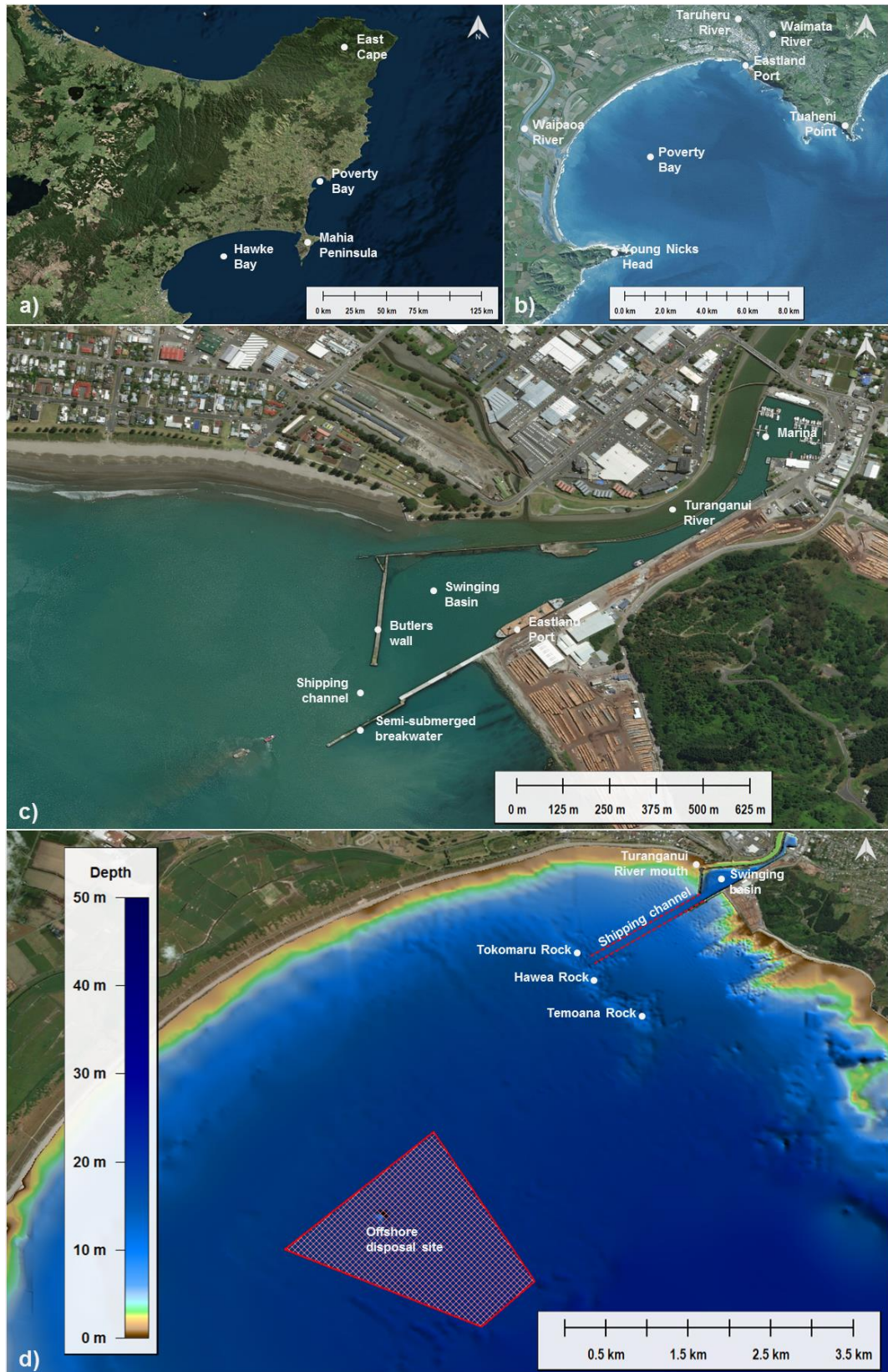


Figure 1.1 Maps showing the location of Poverty Bay (a and b), and Eastland Port (c) with the locations used in the present study. Both offshore disposal and shipping channel are indicated on top of the bathymetry in (d).

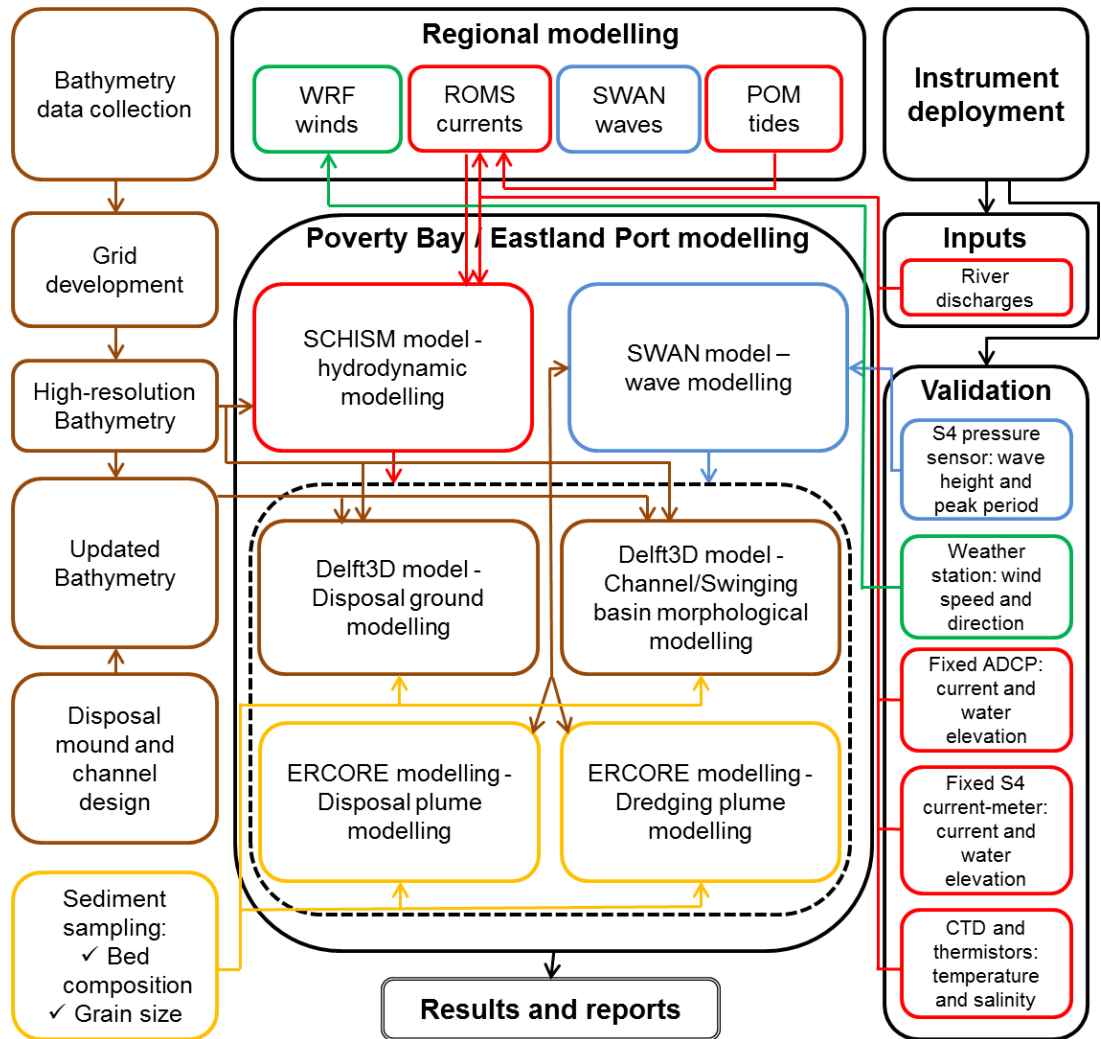


Figure 1.2 Flow chart showing the numerical modelling process for the study. Red lines indicate hydrodynamics; blue indicate waves; green indicate wind; brown indicate bathymetry; and yellow lines indicate sediments.

2. MODEL METHODS

2.1. Bathymetry

Bathymetry is an essential requirement for coastal numerical modelling. MetOcean Solutions has compiled an extensive national and regional bathymetric dataset derived from Electronic Navigation Charts (ENC). These datasets were updated with hydrographic surveys carried out within Eastland Port and the surroundings. Specialist data manipulation tools have been used to allow the merging, interpolation and QA of raw bathymetry data when establishing numerical model domains. Note that GEBCO data (Becker et al., 2009) was also used to characterise the deepest areas.

Water depth in the regional hydrodynamic models was derived from a 500 m gridded bathymetry shown in Figure 2.1 (top). A 5 x 5 m gridded bathymetry (Figure 2.1, bottom) was specifically created over Poverty Bay to interpolate to the computational grids in both ROMS and SCHISM models.

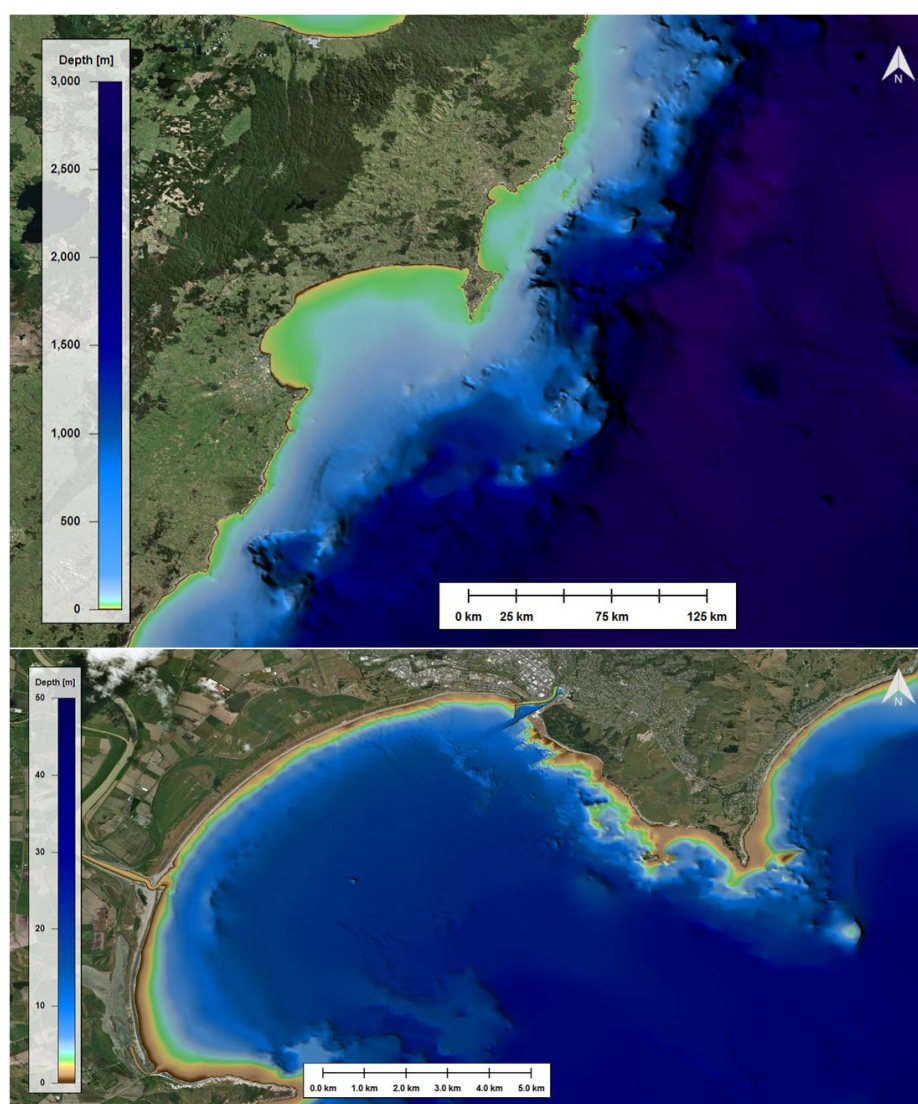


Figure 2.1 Map showing both the 500 x 500 m (top) and the 5 x 5 m (bottom) gridded bathymetries used to interpolate the water depth to the computational grid in ROMS and SCHISM.

2.2. ROMS model

The industry standard hydrodynamic model Regional Ocean Modelling System (ROMS, Haidvogel et al., 2008) has been used to recreate a 10-year regional hindcast. ROMS is widely used in the scientific and commercial consultancy communities at ocean basin, regional and coastal scales. ROMS has a curvilinear horizontal coordinate system and solves the hydrostatic, primitive equations subject to a free-surface condition. The terrain-following vertical coordinate system results in accurate modelling of shelf seas with variable bathymetry, allowing the vertical resolution to be inversely proportional to the local depth. Besides tidal and wind-driven currents, ROMS resolves frontal structures and baroclinic pressure gradients. Vertical mixing can be resolved by different separate turbulent closure schemes that accommodate shallow and deep water dynamics.

2.3. SCHISM model

The unstructured-grid FE SCHISM¹² model was nested within ROMS to increase the available resolution and more accurately account for complex topographical features (rocky reef etc., see Figure 1.1) in the relatively shallow Poverty Bay environment.

SCHISM is a prognostic finite-element unstructured-grid model designed to simulate 3D baroclinic, 3D barotropic or 2D barotropic circulation. The barotropic mode equations employ a semi-implicit finite-element Eulerian-Lagrangian algorithm to solve the shallow-water equations, forced by relevant physical processes (atmospheric, oceanic and fluvial forcing). A detailed description of the SCHISM model formulation, governing equations and numerics, can be found in Zhang and Baptista (2008).

The SCHISM model is physically realistic, in that well-understood laws of motion and mass conservation are implemented. Therefore, water mass is generally conserved within the model, although it can be added or removed at open boundaries (e.g. through tidal motion at the ocean boundaries or fluvial discharges) and water is redistributed by incorporating aspects of the real-world systems (e.g. bathymetric information, forcing by tides and wind and density driven currents). The model transports water and other constituents (e.g. salt, temperature, turbulence) through the use of triangular volumes (connected 3-D polyhedrons).

The FE triangular grid structure used by SCHISM has resolution and scale benefits over other regular or curvilinear based hydrodynamic models. SCHISM is computationally efficient in the way it resolves the shape and complex bathymetry associated with estuaries, and the governing equations are similar to other open-source models such as Delft3D and ROMS. SCHISM has been used extensively within the scientific community^{3,4} where it forms the backbone of operational systems used to nowcast and forecast estuarine water levels, storm surges, velocities, water temperature and salinity⁵.

¹ <http://ccrm.vims.edu/schism/>

² http://www.ccrm.vims.edu/w/index.php/Main_Page#SCHISM_WIKI

³ http://www.stccmop.org/knowledge_transfer/software/selfe/publications

⁴ http://ccrm.vims.edu/schism/schism_pubs.html

⁵ https://tidesandcurrents.noaa.gov/ofs/creofs/creofs_info.html

2.4. Modelling setup

2.4.1. ROMS domain setup

The 10-year ROMS hindcast was undertaken using a three-level nested downscaling approach in order to adequately transfer offshore energy gradually and realistically from the larger to smaller nested domains, and to properly resolve the flow associated with local and remote forcing (e.g. Figure 2.2, Table 2.1).

Details of each of the model domains, including bathymetry, horizontal resolution, number of vertical layers, forcing and associated model spin-up periods are provided in Table 2.1.

The New Zealand scale ROMS parent domain (NZ-ROMS) has a spatial resolution of ~8 km, with 24 vertical layers, and encompasses the entire New Zealand landmass (Figure 2.2, a). Higher resolution nested domains encompass the central East Coast and Poverty Bay (e.g. Figure 2.2, Table 2.1, Gisborne-ROMS and PB-ROMS respectively).

The Gisborne-ROMS model domain extended for approximately 125 – 250 km offshore from South East Cape to South Hawkes Bay (Figure 2.2, b), with 1 km horizontal resolution and 23 vertical levels. The resolution of the model domain allowed for the more accurate parametrisation of the East Cape Current and other meso-scale hydrodynamic features, including resolving in more detail bathymetric controls on shelf circulation near Hawke Bay and Mahia Peninsula.

The PB-ROMS model domain has a horizontal resolution of 150 m and 13 vertical layers. The domain centres on the Poverty Bay region (Figure 2.2, b). The entrance to Poverty Bay is influenced by large and meso-scale hydrodynamics from the open ocean, as well as mixing processes and water discharges from the Waipaoa and Turanganui rivers. The grid extension and domain was chosen to optimise the ability of the model to resolve this complex physical system, and avoiding possible boundary artefacts, whilst maintaining a reasonable computational runtime.

Table 2.1 Relevant characteristics of ROMS domains.

Model Settings	NZ	GISBORNE	POVERTY BAY
Horizontal resolution	0.08 deg.	0.01 deg.	0.0015 deg.
	8 km	1 km	150 m
Vertical S-layers	24	23	13
Tidal forcing	No	No	Yes
River forcing	No	No	Yes
θ_s, θ_b stretching parameters	5 ; 0.4	5 ; 0.1	3 ; 0.1
Baroclinic time step	120 s	60 s	10 s
Minimum depth	20 m	5 m	3 m
Maximum depth	5000 m	6500 m	1500 m
Maximum bathymetry slope	0.2	0.2	0.2
Atmospheric forcing	WRF 12 km	WRF 12 km	WRF 12 km
Spin-up time	5 years	1 month	2 months

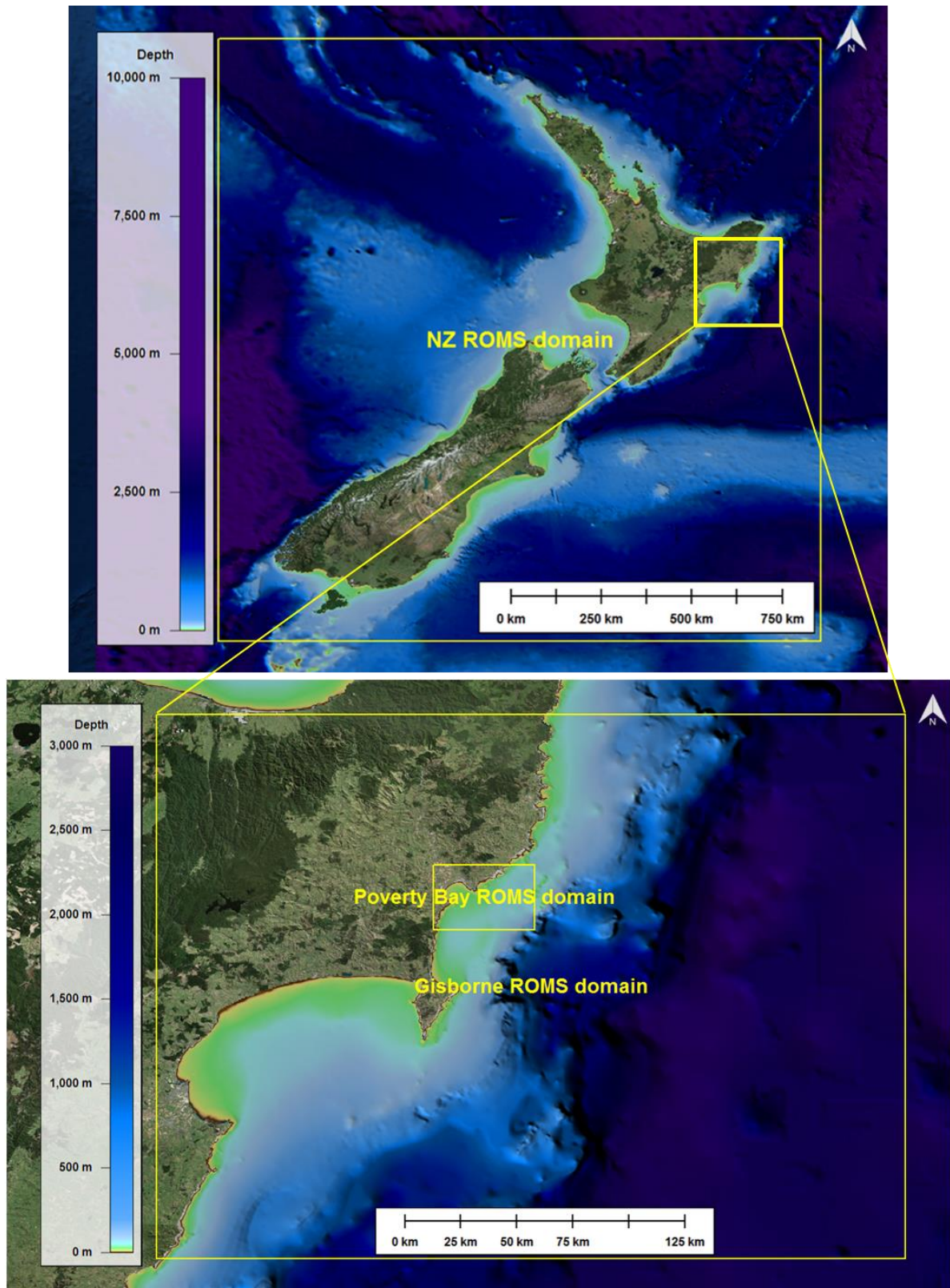


Figure 2.2 Map showing the downscaling approach used to adequately transfer the energy gradually from larger to smaller scales. Yellow rectangles indicate the ROMS domains implemented in the numerical modelling process. NZ, Gisborne and Poverty Bay ROMS grids are characterised by 8 km, 1 km and 150 m resolutions, respectively. Details specific to each set-up are presented in Table 2.1.

2.4.2. SCHISM domain setup

The SCHISM model domain resolution was optimised to ensure replication of the salient hydrodynamic processes. The resolution ranged from 150 m at the offshore boundary to 5 m in shallow water. The model domain was refined around key features, including within Eastland Port, along the shipping channel, within the associated river systems and in areas with complex topography (i.e. Tokomaru, Hawea and Temoana Rocks and the rocky reef shore line). The triangular elements of the model domain meshes are shown in Figure 2.3 and associated bathymetries are presented in Figure 2.4.

For the 3D model simulations, the vertical discretisation of the water column consisted of a Localized Sigma Coordinate system with Shaved Cell (LSC²), a type of terrain-following layers as described in Zhang et al., (2015). The model was configured with a number of sigma layers ranging from 4 in shallow waters to 12 in deep waters near the open boundary. A vertical section showing both the sigma layers and the water depths along the navigation channel is presented in Figure 2.5.

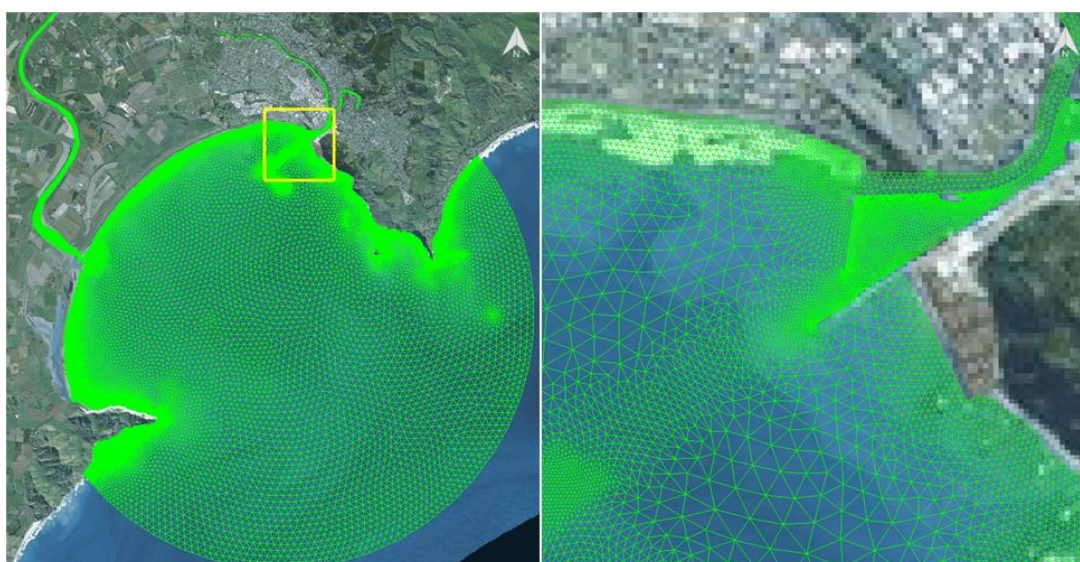


Figure 2.3 Unstructured mesh-grid used in SCHISM to simulate the hydrodynamics over Poverty Bay (left) and Eastland Port (right)

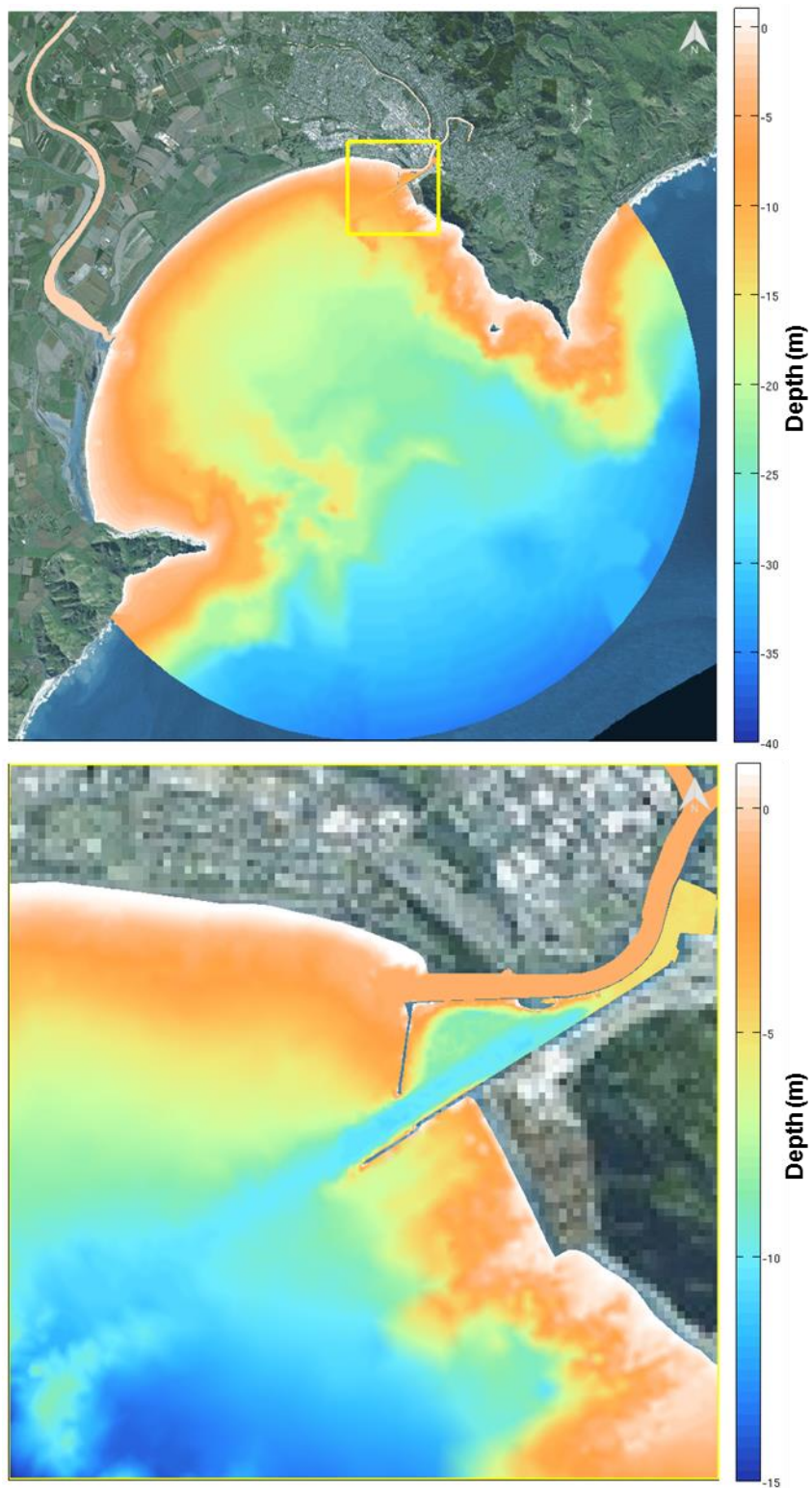


Figure 2.4 Model bathymetries (below mean sea level) over Poverty Bay (left) and Eastland Port (right).

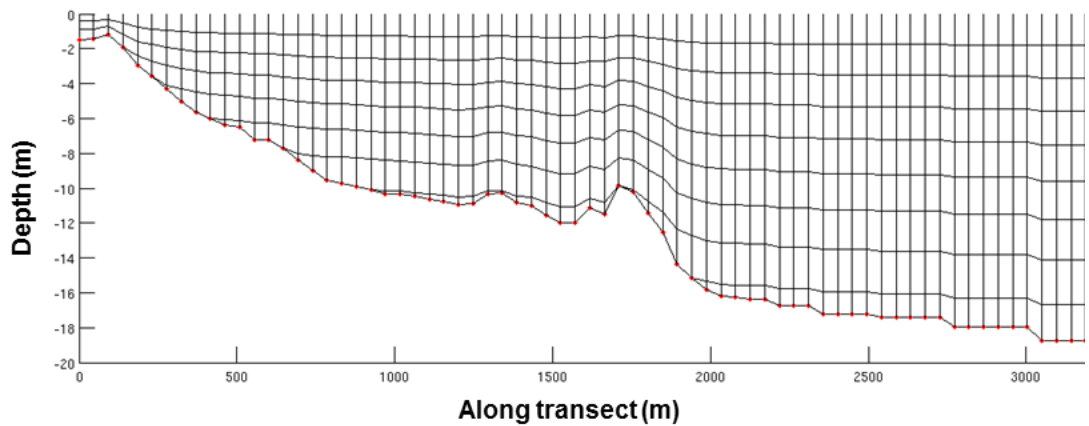


Figure 2.5 Section from the port entrance, and along the navigation channel showing the LSC2 grid used in this study.

2.5. Atmospheric forcing

MetOcean Solutions maintains an up-to-date 12 km resolution New Zealand atmospheric hindcast reanalysis from 1979 to 2016 using the Weather and Research Forecasting (WRF) model and deriving boundary conditions from the global CFSR product used to initialise and force NZ ROMS. The improvement in resolution from the 35 km of CFSR adds accuracy and variability to the atmospheric fields that force ROMS, especially over coastal margins where topography is known to substantially change the large-scale wind patterns and local responses. WRF reanalysis prognostic variables such as winds, atmospheric pressure, relative humidity, surface temperature, long and short wave radiation, and precipitation rate were used at hourly intervals to provide air-sea fluxes to force ROMS in all domains, using a *bulk flux* parameterization (Fairall et al., 2003), and SCHISM.

2.6. Tidal forcing

The widely used tidal constituents sourced to force regional and coastal domains in hydrodynamic models - the Oregon State University Tidal Inverse Solution (OTIS, Egbert and Erofeeva, 2002) – is relatively coarse for direct use in New Zealand coastal domains. Therefore, tidal constituents from the harmonic analysis of a long term 2D Princeton Ocean Model (POM, Mellor, 1998) tidal simulation with 5 km horizontal resolution were used to derive tidal boundaries for the ROMS model. The NZ-POM domain was forced at the open boundaries by tidal elevation and current harmonic constituents derived from the OTIS Pacific Ocean solution⁶. The PB-ROMS domain was forced at the open boundary by elevation and current constituents derived from the POM 2D simulation. Tidal boundary conditions for the SCHISM model were derived from constituents defined from a 1-year PB-ROMS hindcast the 1-hr sampling intervals. For all cases, the tide velocities were interpolated in 3D assuming a logarithmic velocity profile.

⁶ <http://volkov.oce.orst.edu/tides/PO.html>

2.7. Open boundary conditions

High frequency (6-hourly for NZ and 3-hourly for Gisborne-ROMS and PB-ROMS domains) open boundary 3D mass and velocity fields were defined for all ROMS domains. Passive/active prescriptions were applied for all 3D variables at the open boundaries, where a radiation scheme was applied when outflows were estimated by the ROMS algorithms. Bi-dimensional velocities and surface elevation were treated with *Flather* and *Chapman* schemes, respectively, to account for the fast propagating tidal oscillations. Nudging conditions were applied to incoming flows through open boundaries to simulate tri-dimensional transports and Temperature – Salinity inputs from external sources. This setting ensures the contributions of the ECC to the smaller scales near Poverty Bay are factored in.

The SCHISM open-boundary residual velocities, water elevations, salinity and temperature were prescribed from the 3D PB-ROMS domain at 1h interval.

2.8. River forcing

Discharge records of Waipaoa, Waimata and Taruheru rivers measured between 1973 and 2017 by NIWA were processed to force the PB- ROMS and SCHISM domains. Data were first resampled every 3 hours. Thereafter, monthly climatological averages were extracted from these long-term datasets to support the reconstruction of the complete river discharge time series over the simulated period (as a gap filling technique). The time series of the Turanganui river discharge adjacent to Eastland Port was derived by combining both the Waimata and the Taruheru river discharges. Turanganui and Waipaoa river discharge statistics are presented in Table 2.2 to Table 2.5.

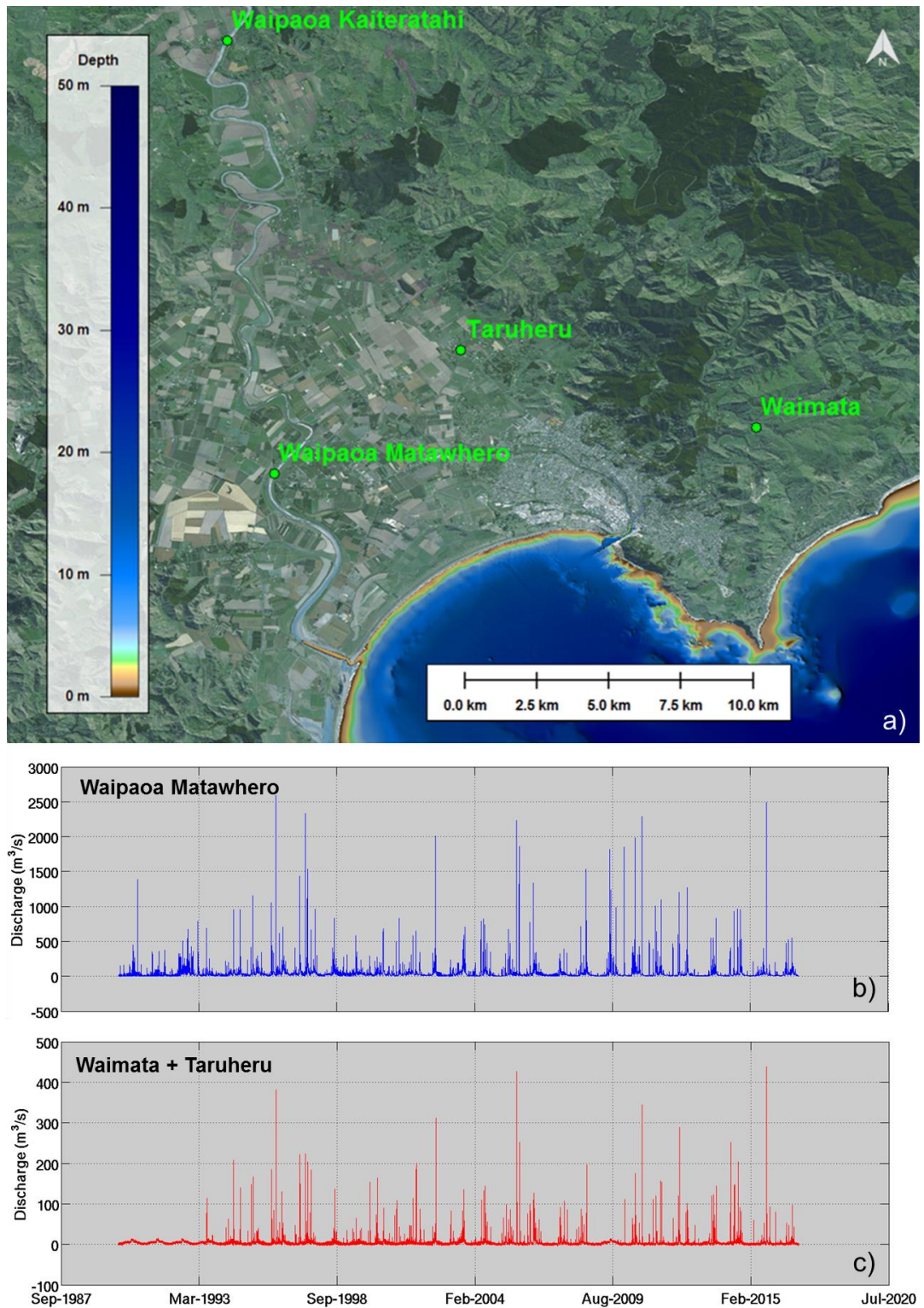


Figure 2.6 Time series of 3-hourly river discharges within Poverty Bay between 1990 and 2016. (a) locations where river discharge and water elevation data were collected by NIWA, (b) Waipaoa river discharge at Matawhero used in the ROMS model and (c) sum of the Waimata and Taruheru river discharge data used in the ROMS model. Data gaps in the measured time series were filled using monthly climatological averages.

Table 2.2 Annual and monthly Turanganui river discharge statistics calculated from combined Waimata and Taruheru river discharges.

	Turanganui River discharge (m ³ .s ⁻¹)								
	min	mean	std	p10	p50	p90	p95	p99	max
Jan	0.02	0.86	4.66	0.04	0.20	1.20	1.93	14.23	193.87
Feb	0.02	1.37	5.03	0.05	0.42	2.52	4.15	16.17	128.65
March	0.03	2.65	11.37	0.05	0.42	4.02	8.55	52.93	226.01
April	0.03	5.76	22.44	0.07	0.74	9.31	22.75	107.82	417.99
May	0.04	2.91	7.76	0.07	0.82	6.46	11.85	37.06	172.49
June	0.05	4.25	11.51	0.23	1.29	8.61	15.35	49.68	225.83
July	0.06	9.02	18.29	1.05	3.96	18.32	30.29	114.83	209.31
Aug	0.08	7.03	16.08	0.94	2.64	12.75	29.90	75.89	329.11
Sept	0.11	7.67	20.77	0.65	2.21	19.02	29.91	82.29	518.10
Oct	0.03	4.28	18.43	0.04	1.36	6.82	11.20	54.53	455.97
Nov	0.01	1.95	7.26	0.04	0.74	3.26	5.05	23.88	257.69
Dec	0.01	0.90	4.42	0.04	0.29	1.23	2.60	11.40	171.72
1993	0.16	4.43	12.59	0.38	1.87	5.84	8.72	88.49	116.53
1994	0.04	4.75	14.90	0.11	1.40	8.60	14.41	70.38	209.31
1995	0.04	5.85	15.16	0.15	1.73	10.78	24.94	90.27	172.49
1996	0.01	5.92	20.95	0.01	1.22	12.28	25.11	63.52	417.99
1997	0.02	10.95	29.63	0.30	3.17	17.57	45.78	187.26	226.01
1998	0.03	2.20	11.77	0.05	0.15	2.46	5.73	49.91	143.67
1999	0.11	4.42	11.88	0.25	1.45	9.23	17.44	39.52	171.72
2000	0.14	3.60	12.74	0.51	1.00	4.90	11.86	70.17	168.44
2001	0.17	6.20	14.49	0.97	2.62	11.62	21.86	78.93	205.46
2002	0.13	2.87	9.11	0.28	0.71	6.72	11.31	27.46	329.11
2003	0.12	6.90	12.46	0.39	2.40	19.24	28.98	63.22	140.37
2004	0.20	5.01	13.14	0.30	1.23	10.40	19.83	71.97	155.37
2005	0.11	5.94	20.43	0.24	2.19	10.01	18.71	67.06	455.97
2006	0.05	5.97	12.30	0.22	1.86	15.08	26.05	66.31	139.50
2007	0.05	3.05	7.62	0.15	0.72	7.17	13.26	37.26	109.33
2008	0.06	2.75	9.02	0.08	0.57	5.79	9.84	38.19	200.28
2009	0.04	1.44	1.69	0.09	0.73	3.77	4.65	7.51	13.16
2010	0.03	4.47	17.66	0.04	1.00	7.17	14.77	71.12	360.81
2011	0.02	2.81	10.34	0.03	0.55	5.10	10.36	38.58	164.57
2012	0.02	4.40	16.88	0.04	0.72	7.98	18.43	70.56	294.44
2013	0.04	2.55	10.34	0.04	0.07	5.03	11.93	51.91	146.11
2014	0.04	5.81	16.69	0.05	0.81	13.16	26.02	78.80	296.71
2015	0.12	3.61	15.45	0.25	1.01	6.08	11.97	46.98	518.10
2016	0.16	3.06	6.81	0.35	1.50	5.35	9.55	40.27	103.00
2017	0.11	0.74	1.47	0.14	0.20	1.75	3.25	7.93	14.16
All	0.01	3.86	13.70	0.05	0.89	7.14	14.39	56.36	518.10

Table 2.3 Monthly Waipaoa river discharge statistics at Matawhero.

	Waipaoa River discharge (m ³ .s ⁻¹)								
	min	mean	std	p10	p50	p90	p95	p99	max
Jan	-0.00	18.38	47.97	3.40	7.72	37.06	58.97	196.74	1341.53
Feb	0.00	18.24	54.31	3.17	7.49	33.76	53.61	220.50	1907.00
March	0.00	44.61	223.43	2.87	10.37	71.66	130.05	530.70	5272.67
April	0.00	57.55	157.00	3.57	18.17	109.11	197.85	765.01	4382.97
May	0.00	44.28	90.56	6.42	19.25	91.49	139.53	491.12	1236.49
June	0.00	58.83	117.55	11.42	28.78	110.27	186.84	549.00	3122.16
July	0.01	89.76	148.32	16.81	49.78	175.40	275.58	855.31	2107.19
Aug	0.01	76.39	127.61	19.49	40.84	144.60	236.44	601.36	2055.63
Sept	0.01	83.60	178.64	12.93	38.51	174.83	309.00	669.87	6518.73
Oct	0.01	47.79	99.11	9.66	25.05	91.53	135.64	436.95	3064.73
Nov	-0.00	27.15	75.62	7.23	15.47	49.03	71.07	186.01	2685.22
Dec	0.00	21.35	58.08	4.92	10.27	38.70	71.57	176.58	1941.99

Table 2.4 Annual Waipaoa river discharge measured at Matawhero – Part 1

	Waipaoa River discharge (m ³ .s ⁻¹)								
	min	mean	std	p10	p50	p90	p95	p99	max
1973	0.38	25.94	76.25	1.09	4.48	46.09	116.20	414.39	1073.60
1974	1.78	53.24	77.02	2.69	26.41	147.08	209.70	355.11	1002.39
1975	2.85	41.12	55.07	5.59	25.69	86.12	126.33	326.32	490.40
1976	6.62	75.69	150.38	11.23	38.82	140.58	234.71	704.92	2275.41
1977	5.13	62.99	107.29	8.31	23.56	153.85	269.93	563.77	986.70
1978	4.33	42.59	84.83	6.03	14.85	90.22	139.78	528.56	796.65
1979	2.58	54.01	63.94	5.19	32.92	131.06	183.65	307.32	564.00
1980	6.00	75.52	153.84	13.45	31.32	138.26	301.84	849.70	1941.99
1981	5.19	64.93	97.14	7.75	29.58	156.00	232.94	491.13	966.61
1982	2.95	42.15	123.65	5.71	20.79	71.74	115.88	284.91	2111.94
1983	0.72	23.91	44.12	1.30	13.74	50.52	81.90	186.59	608.92
1984	3.90	57.55	130.56	8.15	26.98	112.44	195.14	604.16	1986.86
1985	2.77	70.22	143.67	6.38	34.08	143.49	246.30	669.19	1897.29
1986	0.88	27.45	67.12	1.63	18.51	45.69	79.06	320.87	1067.97
1987	2.77	73.63	151.18	12.57	28.11	130.85	253.45	978.63	1162.74
1988	0.90	177.50	534.85	20.12	77.85	197.49	449.49	3015.71	6518.73
1989	-0.00	105.78	193.48	0.18	30.97	378.69	564.55	821.26	1883.14
1990	0.00	37.64	112.14	0.01	4.59	86.96	194.09	529.71	1423.57
1991	-0.00	21.17	48.48	0.03	3.41	58.94	116.09	257.22	386.07
1992	0.01	65.43	90.23	0.07	28.84	167.90	240.18	418.02	1408.86
1993	1.07	38.50	72.92	6.31	14.60	87.34	133.81	371.17	1007.98

Table 2.5 Annual Waipaoa river discharge measured at Matawhero – Part 2

	Waipaoa River discharge (m ³ .s ⁻¹)								
	min	mean	std	p10	p50	p90	p95	p99	max
1994	0.77	48.53	100.12	4.59	28.48	94.22	132.94	442.32	1576.44
1995	0.53	61.39	120.70	6.32	29.76	122.47	186.38	892.19	1236.49
1996	1.23	83.43	223.78	9.21	37.05	147.88	239.97	934.74	4382.97
1997	1.95	109.61	226.52	11.20	50.37	184.37	339.22	1331.04	3122.16
1998	0.60	51.27	77.10	5.03	26.77	105.70	163.04	366.77	1018.82
1999	0.95	45.14	50.40	5.72	36.91	83.89	114.95	261.07	729.74
2000	2.13	42.36	49.40	7.75	28.73	82.38	119.47	266.05	701.30
2001	4.46	55.64	70.29	13.20	37.12	102.83	155.29	407.14	862.70
2002	1.06	50.92	190.03	3.51	13.38	78.44	139.89	1108.74	2055.63
2003	0.79	52.38	72.67	4.68	29.65	125.40	181.25	360.61	771.29
2004	1.98	42.30	79.41	4.07	14.95	98.68	151.45	424.13	841.48
2005	1.27	53.79	233.33	2.62	14.95	65.41	130.56	1123.63	3064.73
2006	0.01	74.71	190.24	3.29	14.83	177.06	379.38	948.46	1781.75
2007	1.00	23.49	39.98	3.02	11.86	43.38	84.15	229.21	450.43
2008	1.00	33.52	85.85	4.99	14.33	59.70	98.79	326.99	2107.19
2009	1.10	43.06	124.52	3.45	13.77	83.77	145.19	619.36	1821.44
2010	3.38	62.16	186.20	6.04	16.81	108.15	193.80	1089.82	2304.84
2011	1.76	35.41	70.80	6.38	18.07	69.33	109.69	319.74	1129.94
2012	4.60	43.86	110.21	7.00	14.94	80.03	183.40	566.86	1295.70
2013	2.32	26.60	57.12	3.71	10.50	58.06	100.37	259.22	841.24
2014	4.20	42.42	86.42	5.91	16.95	89.69	153.21	459.91	983.24
2015	5.01	34.53	105.66	6.71	15.79	59.31	92.08	329.34	2546.88
2016	2.88	33.18	51.07	7.23	16.30	71.27	101.10	308.38	557.22
2017	3.39	51.39	105.98	4.76	21.32	101.46	164.53	692.34	1057.04
All	-0.00	48.76	128.61	5.12	19.55	97.72	160.58	512.49	6518.73

2.9. ROMS model validation methods

The predictive capability of hydrodynamic numerical models applied to a particular system depends on many factors. Although part of the modelling uncertainty is directly linked to the model itself (simplifying assumptions, model limitations, numerical schemes and discretisation, etc.), model inputs (bathymetry, forcing) and non-deterministic features of the system (anthropogenic interactions, abnormal events) play a major role influencing the model performance.

Here we present the framework for validation of the ROMS numerical modelling undertaken in the present study. The calibration and validation consisted of three steps:

1. Definition of initial uncertainties;
2. Evaluation criteria;
3. Comparison between field and model data;

This standard framework aimed to demonstrate the suitability of the model for replicating multi-scale hydrodynamic processes along the eastern continental shelf of Gisborne and within Poverty Bay, as well as to assess the model uncertainty. Assessing uncertainty is particularly important for decision-makers as it places the model results into context and helps the interpretation of the model outputs.

2.9.1. Definition of initial uncertainties

Numerical modelling essentially aims to strike a balance between computational time, numerical stability, and model performance for a particular purpose. Model configuration and input data derived from other numerical models are therefore sources of uncertainty. Here we establish and quantify (where possible) the uncertainty associated with the model configuration and the input data used to force ROMS.

- Model bathymetry and smoothing

Large amounts of data were available because of the numerous coastal studies in Poverty Bay and the adjacent continental shelf. The Electronic Nautical Charts (ENCs) and contemporary single- and multi-beam survey data available are spatially sporadic, with good coverage of areas adjacent to Eastland Port as well as Tokomaru, Hawea, and Temoana rocky reefs. Also well covered are the disposal sites considered for the placement of maintenance dredging volumes. By contrast, the Waipaoa river mouth and the continental shelf at the entrance to Poverty Bay are poorly sampled. Although unquantifiable, the impact of such heterogeneity in the bathymetry data sampling over the study area is expected to be relatively low compared to other limitations of the numerical modelling.

Numerical model instabilities associated with the generation of pressure gradient errors between the terrain-following sigma layers (Beckman & Haidvogel, 1993) will likely create artificial currents in the range 0 – 0.015 m/s along the steepest areas of the domain. This can be mitigated by smoothing the model bathymetry. However, the smoothing process results in a slight loss of model accuracy over the steep area. For this reason, comparisons between measured and model data at several sites outside Poverty Bay were used to quantify the model accuracy over the continental shelf slope. Results from this analysis are presented in Section 3.2.2.

- Atmospheric forcing

The 12 km WRF hindcast used to force the intermediate and high-resolution ROMS domains was validated using measured surface wind data collected at Gisborne Airport. Gisborne Airport is surrounded by mountains and partially sheltered from north-easterly winds by the embayment. For this reason, the Hicks Bay site was also used as control site during the validation process. The Hicks Bay (East Cape) weather station is particularly exposed to coastal winds. Using both sites allowed us to incorporate potential topographic effects on the model accuracy. The wind validation is presented in Section 3.2.1. Additional results are provided in Appendix A.

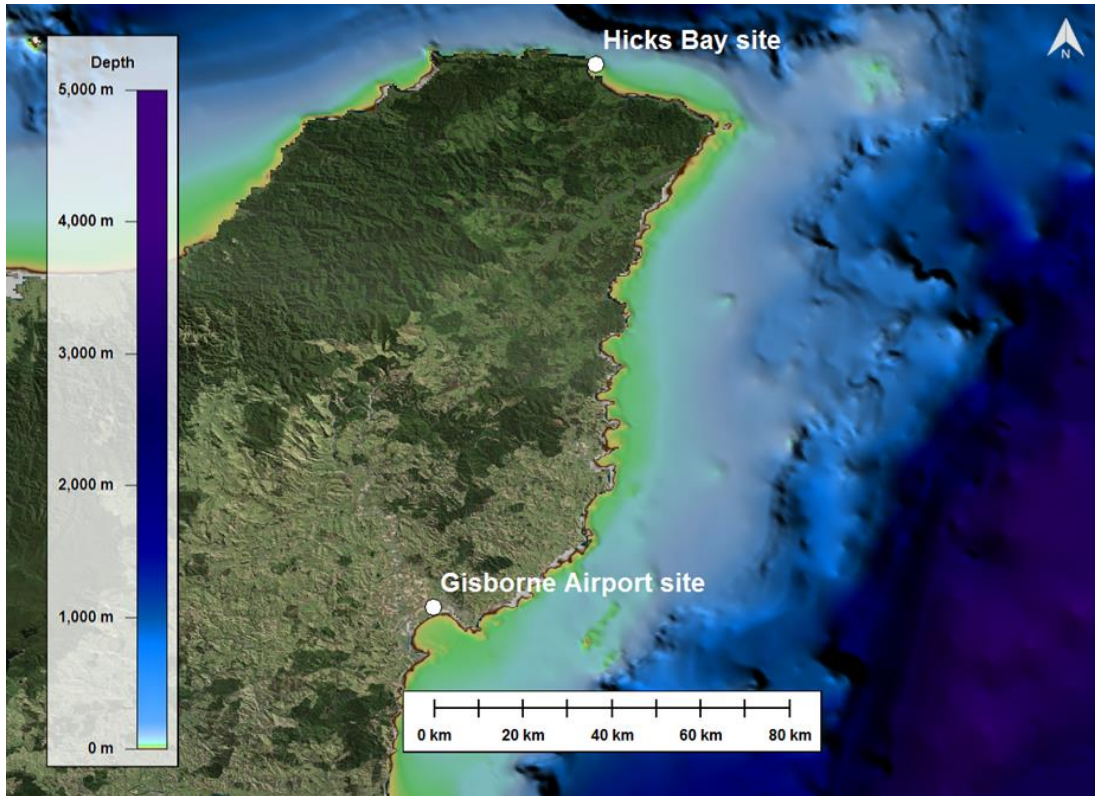


Figure 2.7 Map showing the regional bathymetry of the continental shelf between Gisborne and East Cape. The white dots indicate the sites used to compare hindcast and weather station wind data.

- Tidal forcing

Tidal water elevation and current fields were supplied to the Poverty Bay ROMS boundaries from the 5 km 2D POM tidal hindcast produced by MSL. This product has shown improved validation results in many areas around New Zealand when compared to OTIS (Egbert & Erofeeva, 2002). Because Poverty Bay is a micro-tidal system, the tidal current impact on the hydrodynamics in Poverty Bay is expected to be low.

2.9.2. Evaluation criteria

The predictive skill assessment of the ROMS numerical model was based on two main evaluation criteria:

- The qualitative agreement between significant features of the regional circulation predicted by the model and the expected literature-described patterns.
- The quantitative agreement between model and observations at several sites within the study area. For this purpose, the following quantitative accuracy parameters were calculated from the measured X_m and hindcast, X_h data:

Mean absolute error (MAE):
$$\overline{|x_h - x_m|} \quad (\text{Eq. 2.3})$$

$$\text{Root Mean Square Error (RMSE):} \quad \sqrt{(x_h - x_m)^2} \quad (\text{Eq. 2.4})$$

$$\text{Mean relative absolute error (MRAE):} \quad \frac{|x_h - x_m|}{x_m} \quad (\text{Eq. 2.5})$$

$$\text{Bias:} \quad \overline{x_h - x_m} \quad (\text{Eq. 2.6})$$

$$\text{Scatter Index (SI):} \quad \frac{\sqrt{(x_h - x_m)^2}}{x_h} \quad (\text{Eq. 2.7})$$

Additionally, time series, roses and/or Quantile-Quantile plots were used to assess the agreement between hindcast and measured data.

2.9.3. Comparison between model and literature-described patterns

Poverty Bay is a complex coastal embayment essentially influenced by:

- the inner continental shelf currents;
- river discharge;
- wind upwelling and down-welling;
- vertical mixing due to salinity and temperature gradients; and
- tidal dynamics.

The temporal and spatial variability of these processes posed significant challenges to hydrodynamic modelling. To ensure that ROMS was able to adequately replicate the above processes, we examined the agreement between model and literature-described patterns within Poverty Bay and the surroundings. The procedure for analysing the hydrodynamic patterns in the model focused on three main processes:

- Influence of the inner continental shelf currents on the inner circulation: persistent clockwise and anti-clockwise gyres within Poverty Bay corresponding to northerly and southerly flow shelf currents, respectively.
- Effect of river discharge on the inner circulation: modification and/or interruption of the circulation gyres during moderate to high river discharge events, and extension of south-eastward currents to the continental shelf margin.
- Effect of river discharge and wind-driven upwelling on the mixing processes.

This analysis aimed to divide the bay hydrodynamics into sub-processes allowing better identification and understanding of the potential limitations of the model. The analysis of the agreement between model and literature-described patterns are presented in Section 3.1.

2.9.4. Instrument deployment

Current velocities and water elevations measured by ADCP and S4 current meter within Poverty Bay and the adjacent shelf margin (Figure 2.8) were used to validate the ROMS hydrodynamic hindcast.

ADCP datasets were provided by R.P. Hale (College of Science, Old Dominion University) and A.S. Ogston (School of Oceanography, University of Washington). The datasets consisted of 3D velocity fields sampled at between 0.5 m and 1 m bins vertically within the water column, from the year 2010 (Hale et al., 2014).

Point source UV current velocities were measured using S4 current meters deployed at CM2, CM6 and DW in 1996 and 1998 (Table 2.6). For sites CM2 and DW, water elevation records were used to validate the model.

The instrument deployments, including geographic coordinates, observational durations, samplings, record levels, and water depths, are summarised in Table 2.6. Results of the model performance assessment including accuracy measurements (Eq. 2.3 to 2.7) and plots are provided in Section 3.

Table 2.6 Geographic coordinates, observational durations, samplings, record levels and water depths of the ADCP and S4 current meter deployments over Poverty Bay and the adjacent shelf margin.

Site	Deployment	Coordinates (WGS84)		Observational durations (dd/mm/yyyy)		Vertical references (m - BSL)		Sampling
		Longitude (E)	Latitude (N)	Start date	End date	Level	Water depth	
CM2	S4 CM - 01	178.0077	-38.6819	04/07/1996	10/08/1996	10	11	18-min burst averages every hour
	S4 CM - 02			16/08/1996	28/08/1996			
CM6	S4 CM - 01	177.9637	-38.7181	14/08/1996	28/08/1996	13	14	2-min burst averages every hour
DW ⁽¹⁾	S4 CM - 01	178.0645	-38.7738	09/09/1998	17/10/1998	11.4	33	Three 20 s averages per minute every 5 minutes
	S4 CM - 02			09/09/1998	22/10/1998	31		Five 12 s averages per minute every 5 minutes
NT	ADCP - 01	178.0924	-38.7921	15/01/2010	10/04/2016	Water column	37	6-min burst averages every hour
	ADCP - 02			24/05/2010	05/09/2010			
	ADCP - 03			10/09/2010	09/02/2011			
DT	ADCP - 01	178.1916	-38.8298	15/01/2010	20/05/2010	Water column	72	6-min burst every hour
	ADCP - 03			10/09/2010	05/01/2011			

Notes: (1) The current meters at DW were referred as S4 and GB in Stephens et al. (2001).

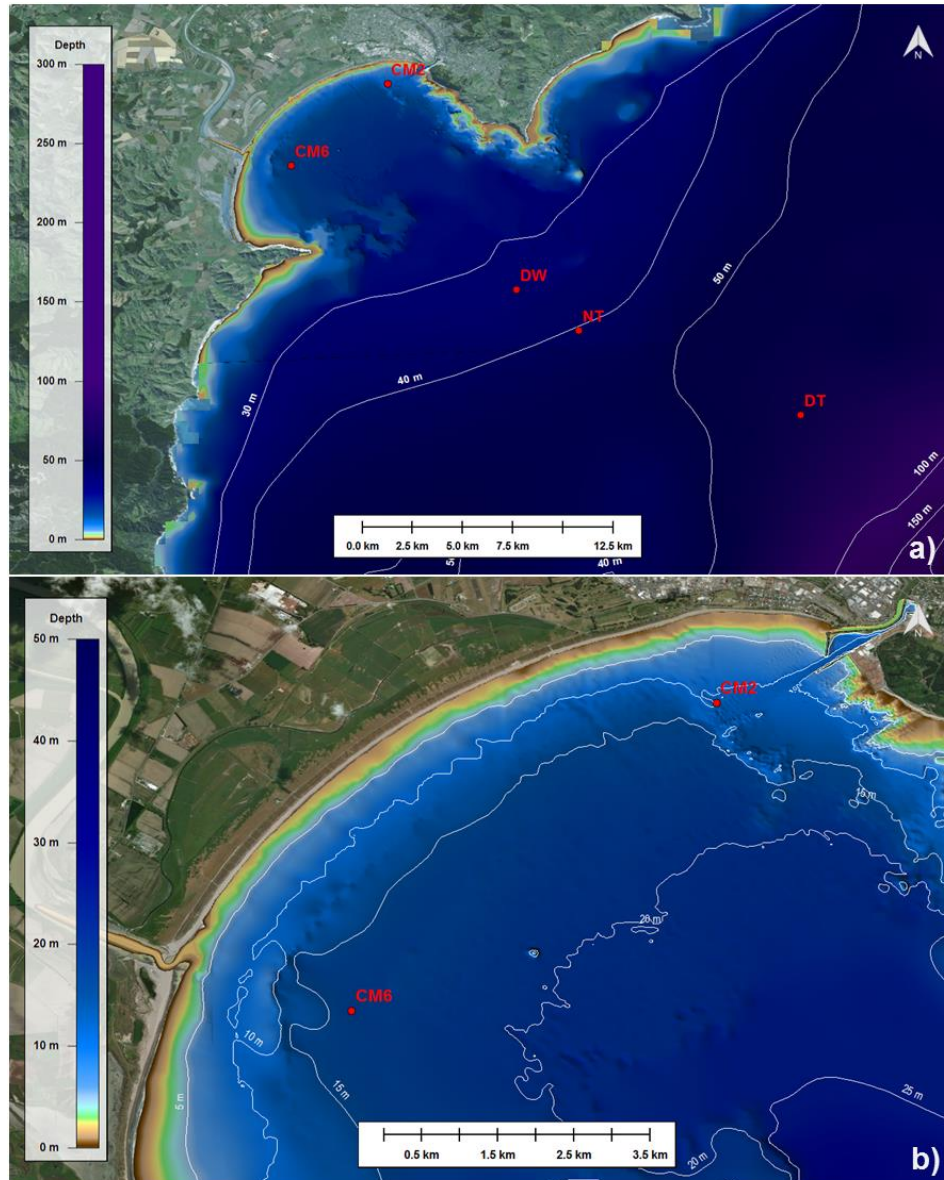


Figure 2.8 Map showing the bathymetry over the Gisborne continental shelf (a) and Poverty Bay (b). The red dots indicate the sites used to validate the ROMS hydrodynamic model against ADCP and S4 current meter data recorded in 1996, 1998 and 2010 (R.P. Hale, Old Dominion University; A.S. Ogston, University of Washington, School of Oceanography).

2.10. SCHISM model validation methods

Due to the spatial coverage of the SCHISM domain (Figure 2.3), the predictive skill assessment of the SCHISM numerical model focused essentially on the comparisons between field and model data at sites CM2 and CM6 (Figure 2.8). The SCHISM model was developed in order to improve the horizontal and vertical resolution of the available hindcast data and to more accurately define their hydrodynamics within the key areas of interest (i.e. at the offshore disposal ground, within the navigation channel and within the port confines). These data are key requirements for the dredge and disposal plume modelling and subsequent morphological modelling.

3. RESULTS

3.1. Qualitative validation

3.1.1. Influence of shelf currents on the inner circulation

During events characterised by southerly flowing shelf currents and low-river discharge, Tuaheni Point at the northern end of Poverty Bay deflects currents into the bay. This induces an anti-clockwise circulation initiated over the deeper area of the bay. At these times, low-velocity inner bay currents have relatively weak velocities. To the south, outgoing currents form a counter coastal current between Southern Poverty Bay and Mahia Peninsula, extending approximately 1 – 8 km offshore. The presence of Mahia Peninsula and the orientation of the coastline cause this recirculation to develop, which in turn pushes away the northward shelf currents (Figure 3.1).

By contrast, northerly flowing shelf currents generate a clockwise gyre in the bay (Figure 3.2). Southward shelf currents are more frequent than northerly flows but comparisons between monthly depth-averaged current fields (see monthly-averaged current fields in Appendix B) indicate that the anticlockwise circulation gyre pattern dominates in the bay. This mechanism is mainly caused by the Coriolis affect, which enhances westward current deflection near Tuaheni Point enhancing the anticlockwise circulation.

More broadly, the predicted effects of the shelf currents on the inner circulation within Poverty Bay are in agreement with the description provided by Black et al. (1997) and Stephens et al. (2001). It is, however, important to note that high river discharges are relatively frequent (see Section 2.5). For this reason, the second stage of the qualitative model validation assessed the influence of moderate to large river discharges on the environment.

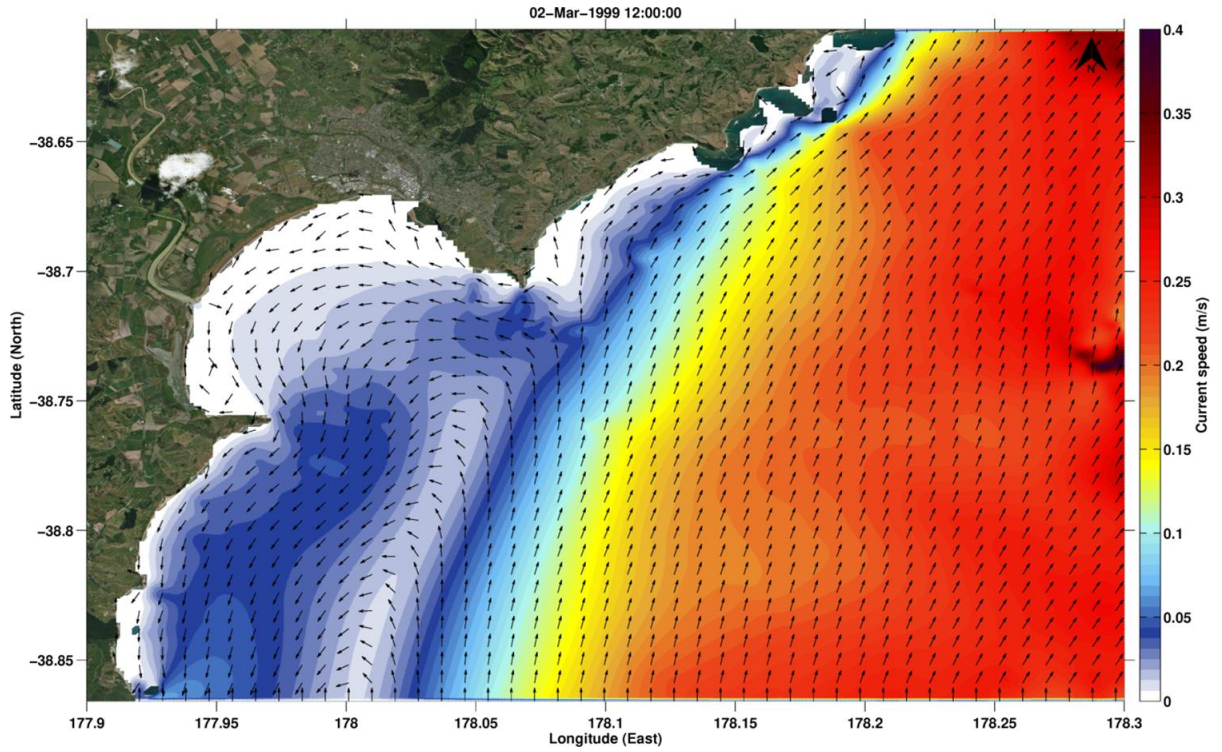


Figure 3.1 Daily depth-averaged current fields predicted by ROMS for March 2nd 1999 within Poverty Bay and over the adjacent continental shelf region.

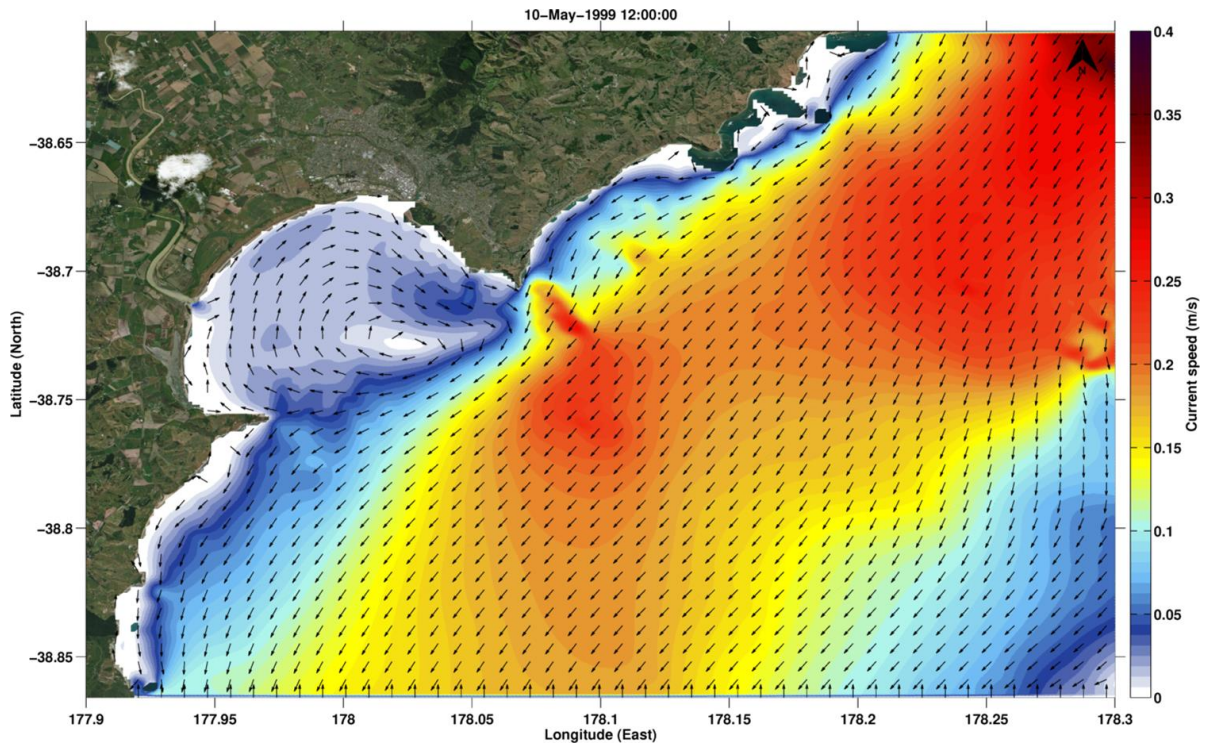


Figure 3.2 Daily depth-averaged current fields predicted by ROMS for March 10th 1999 within Poverty Bay and over the adjacent continental shelf region.

3.1.2. Influence of river discharge on the inner circulation

Both the Waipaoa and Turanganui Rivers (though to a lesser extent) discharge relatively high volumes of fresh water into Poverty Bay, and as such can significantly influence the bay-wide hydrodynamics within this micro-tidal semi-enclosed system.

South-eastward surface currents associated with moderate to strong Waipaoa river discharge generate a complex hydrodynamic system which can extend to the outer parts Poverty Bay. Black et al. (1997) showed that high river discharges dominated the surface currents in the bay even in the presence of strong inner shelf currents. At such times, Black et al. (1997) did not observe any circulation gyre. The present model outputs show similar patterns. While the monthly depth-averaged currents clearly show circulation gyres, the monthly-averaged surface currents are dominated by eastward and south-eastward fluxes (see Figure 3.3 and Figure 3.4), particularly in the vicinity of the Waipaoa River mouth, as described in Bever (2010). The influence of the Turanganui River appears mainly constrained to the northern margin of the bay, although exceptional rainfall events within the catchment area can result in significant surface currents extending to the entrance of the bay.

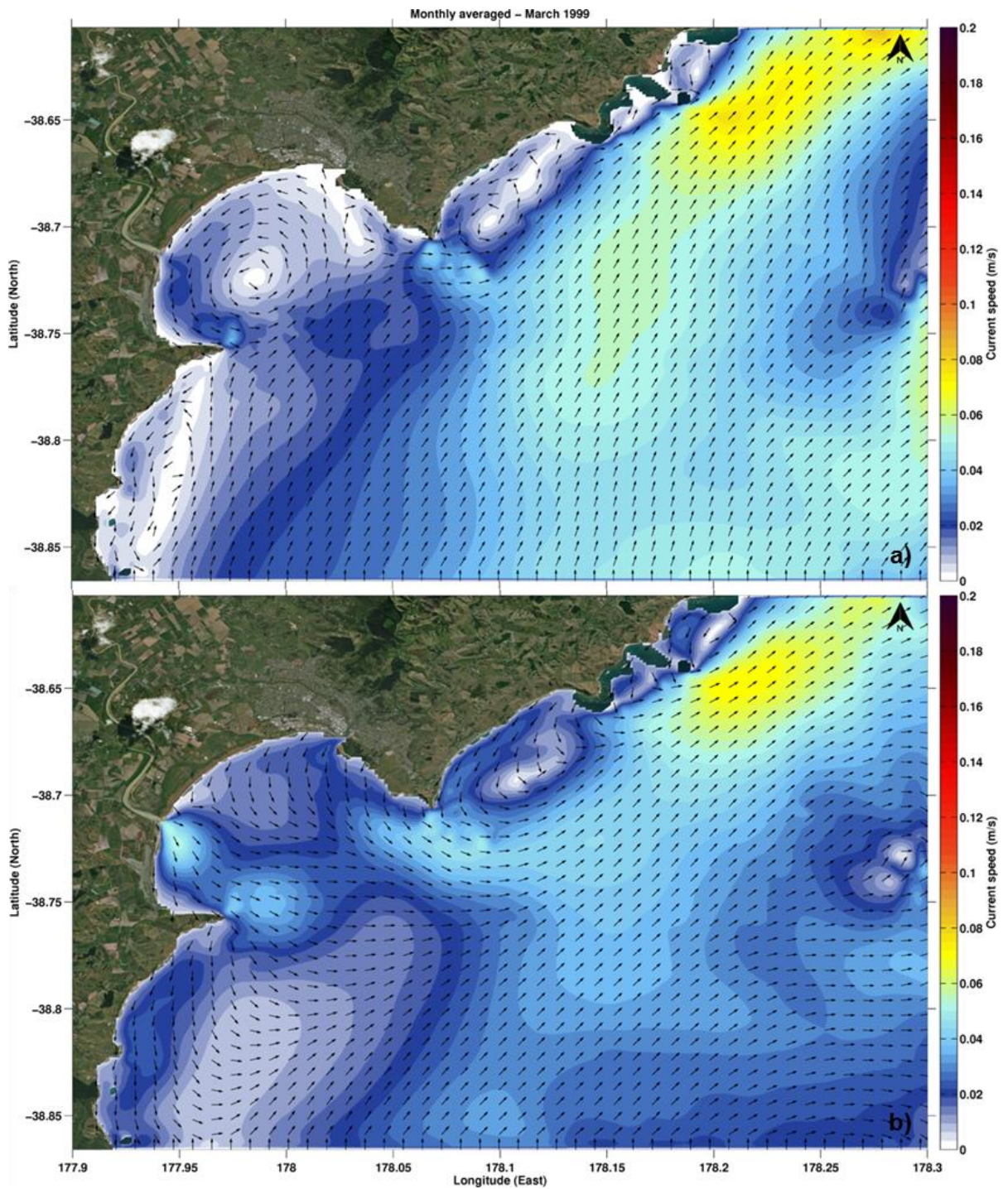


Figure 3.3 Monthly depth-averaged (a) and surface (b) current fields predicted by ROMS for March 1999 within Poverty Bay and over the adjacent continental shelf region.

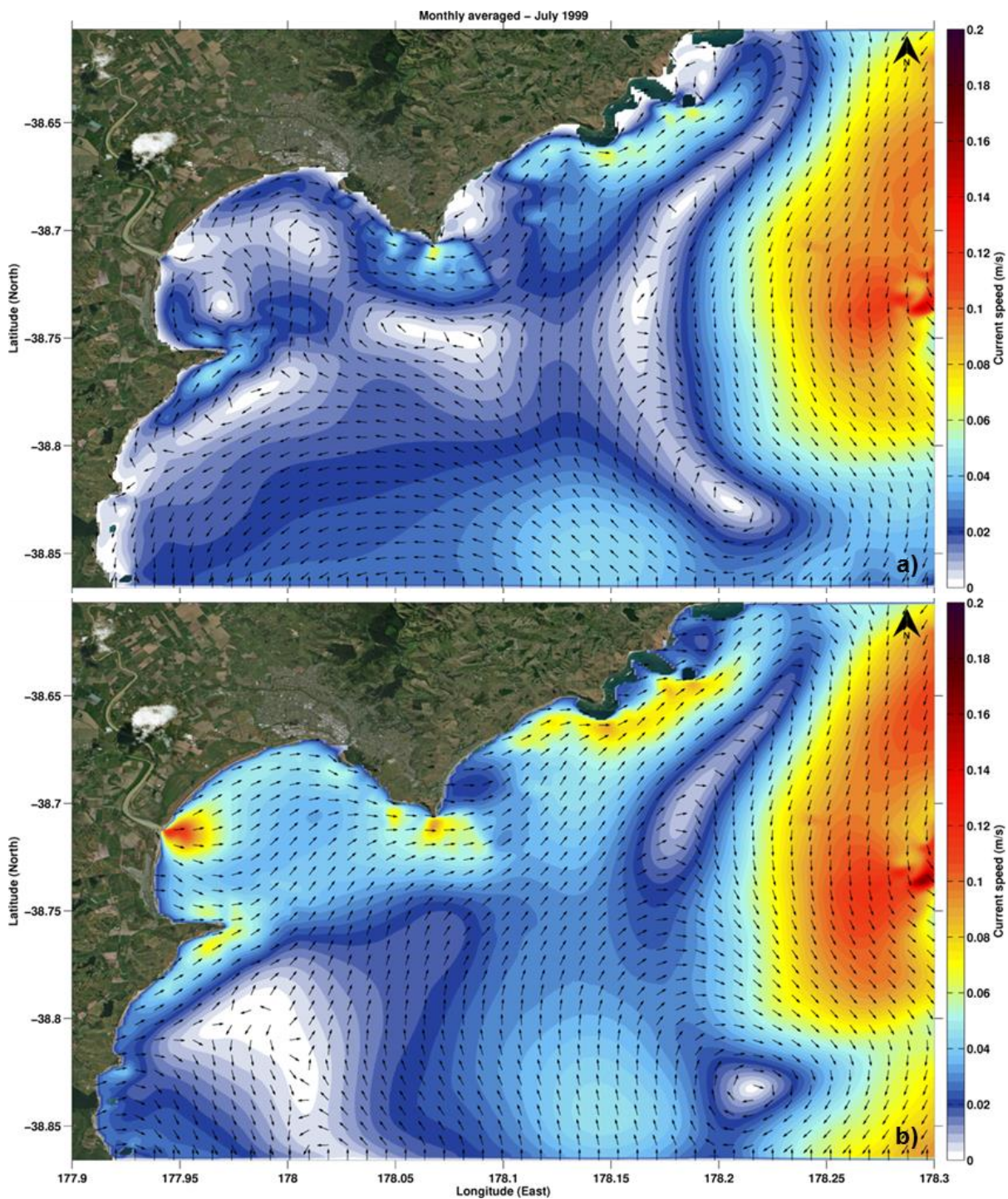


Figure 3.4 Monthly depth-averaged (a) and surface (b) current fields predicted by ROMS for July 1999 within Poverty Bay and over the adjacent continental shelf region.

3.1.3. Mixing processes within Poverty bay

As described by Bever et al. (2011), the fluctuations of salinity and temperature in the bay are controlled by three factors:

- (1) freshwater discharges from the Waipaoa and Turanganui River (though to a lesser extent),
- (2) wind-driven up-welling/down-welling, and
- (3) seasonality

The strong salinity gradient during large river discharge episodes generates density driven mixing processes that affect the hydrodynamics of the bay. The resultant water stratification is mainly constrained to the top 5 m of the water column, and extends horizontally to the continental shelf with a slow decay of the gradient as shown in Figure 3.5 and Figure 3.6.

During NW wind episodes, wind-driven surface offshore currents and onshore bottom currents lead to upwelling along the coast. This mechanism, described in Stephens et al. (2010), is partially replicated by ROMS (Figure 3.7). Directional bias resulting from a 12-km wind hindcast resolution (see Section 3.2.1) limits the occurrence of NW wind and associated upwelling in the model. This limitation is not expected to significantly affect the ability of the model to predict the overall hydrodynamics within Poverty Bay.

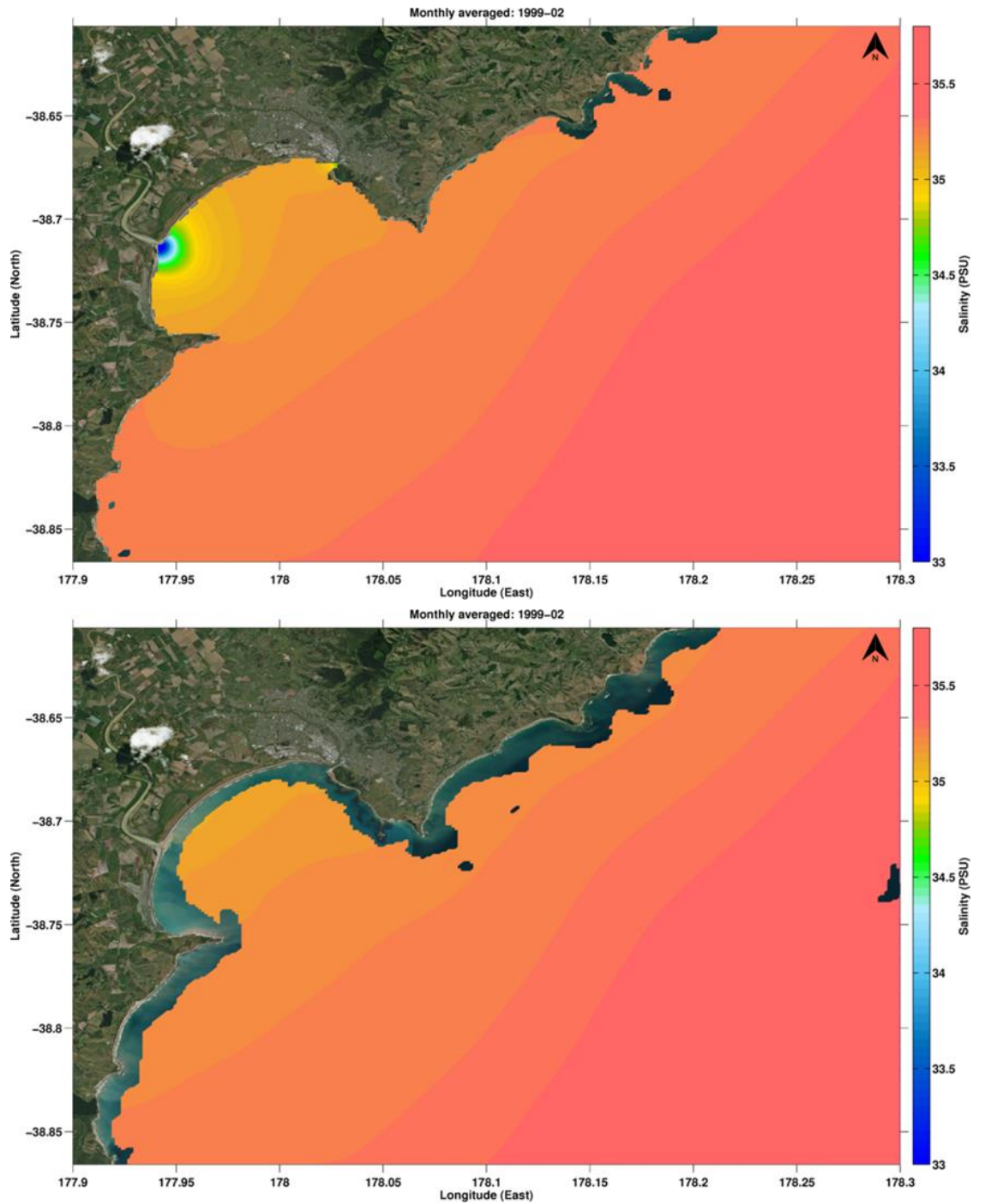


Figure 3.5 Monthly surface (top) and 5 m (bottom) salinity predicted by ROMS for February 1999 within Poverty Bay and over the adjacent continental shelf region.

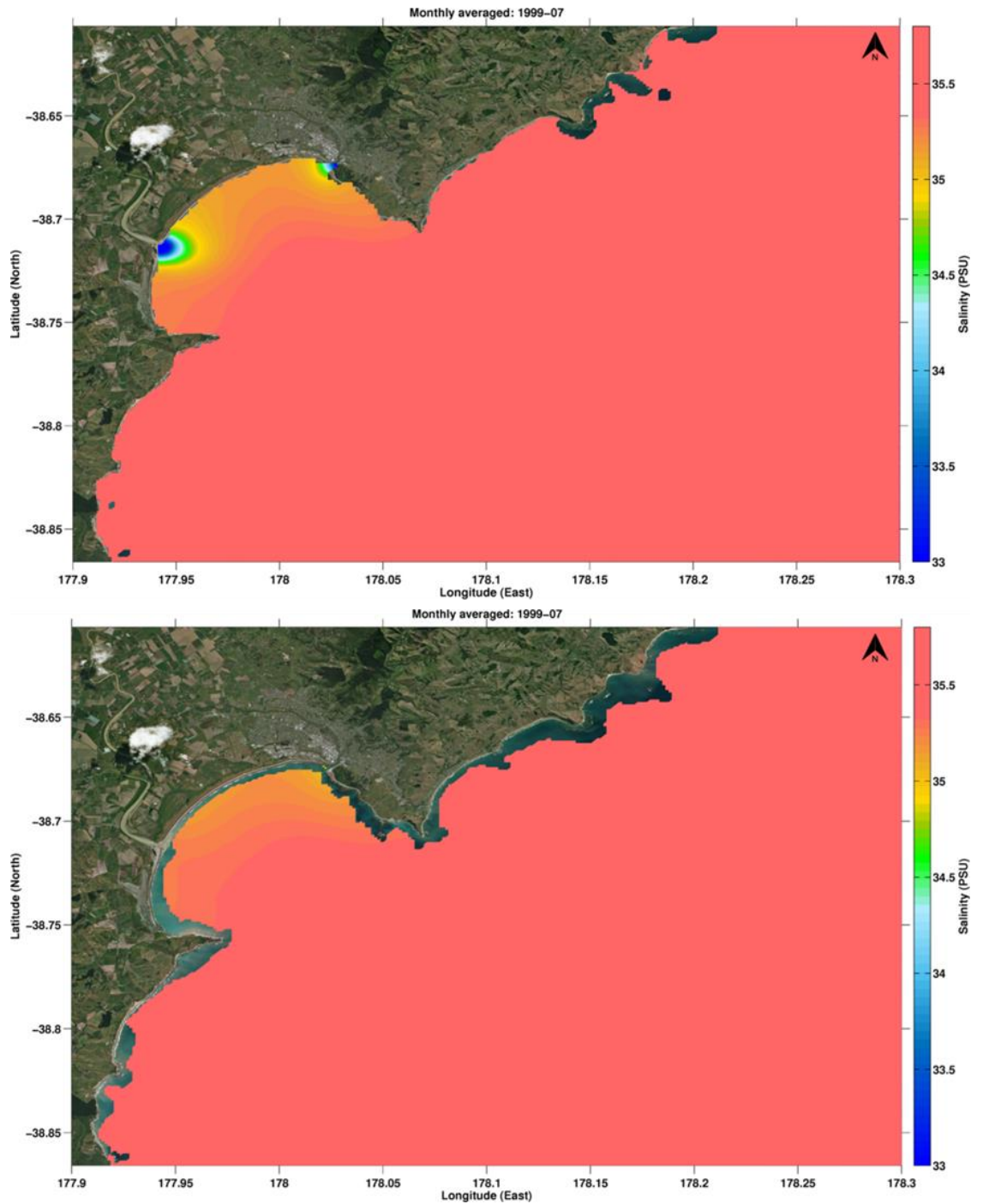


Figure 3.6 Monthly surface (top) and 5 m (bottom) salinity predicted by ROMS for February 1999 within Poverty Bay and over the adjacent continental shelf region.

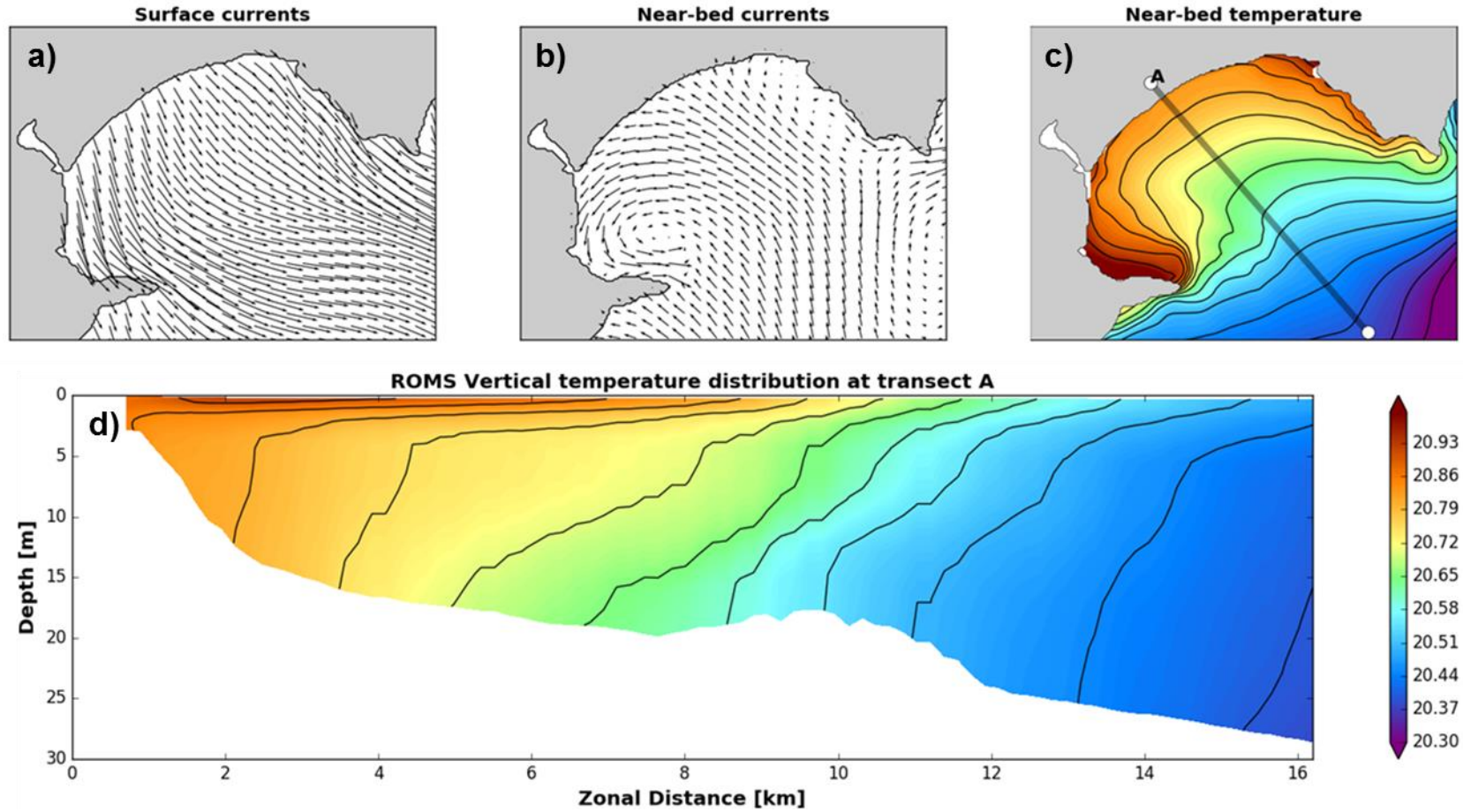


Figure 3.7 Average flow pattern under NW winds influence at Poverty Bay: (a) average surface currents predicted by ROMS during NW wind episodes; (b) average near-bed currents predicted by ROMS during NW wind episodes; (c) position of the transect used to examine the spatial variations of the temperature in ROMS; (d) Average temperature section extracted from the ROMS outputs for NW wind episodes.

3.2. Quantitative validation

3.2.1. Wind climate

Hindcast wind velocities at 10 m used to force the ROMS model were compared against observations from the Gisborne Airport weather station. The time series of model and measured wind speed for the period June 2002 - June 2003 are shown in Figure 3.8.

The quantitative validation (Figure 3.9) showed the model to exhibit a reasonable correspondence with the measured data. On average, hindcast wind speeds were biased slightly high by ~ 0.75 m.s⁻¹, while peak wind speeds were biased slightly low (by 1-2 m.s⁻¹, Table 3.1).

Comparisons of the model and measured wind roses are provided in Figure 3.10 and show a good directional correlation, with predominant NW octant winds in both model and measured data, consistent with the findings of Chappell, (2016).

In general, measured winds at Gisborne Airport tend to be primarily orientated NW/SE. In comparison, modelled winds tend to display more directional variance; due to the topographical sheltering effect afforded by Poverty Bay not being fully captured in the 12 km resolution atmospheric model.

To evaluate if this directional bias was mainly constrained to the Poverty Bay embayment a comparison between the measured and model wind data at Hicks Bay, located at East Cape (Figure 2.7), was undertaken. This area is one of the most exposed locations along the East Coast where measured wind data are available. Measured and model wind roses from Hicks Bay are provided in Appendix A, and show the model data to accurately capture the climatic variability in the wind fields at this more exposed site, suggesting the disparity between modelled and measured wind climates at the Gisborne Airport is due to topographical effects not fully represented within the model.

The effect of not fully capturing the SE events within the wave hindcast in Poverty Bay on the wave and current outcomes (SWAN and ROMS/SCHISM) is not expected to be significantly in terms of quantifying the wave and current climatic variability.

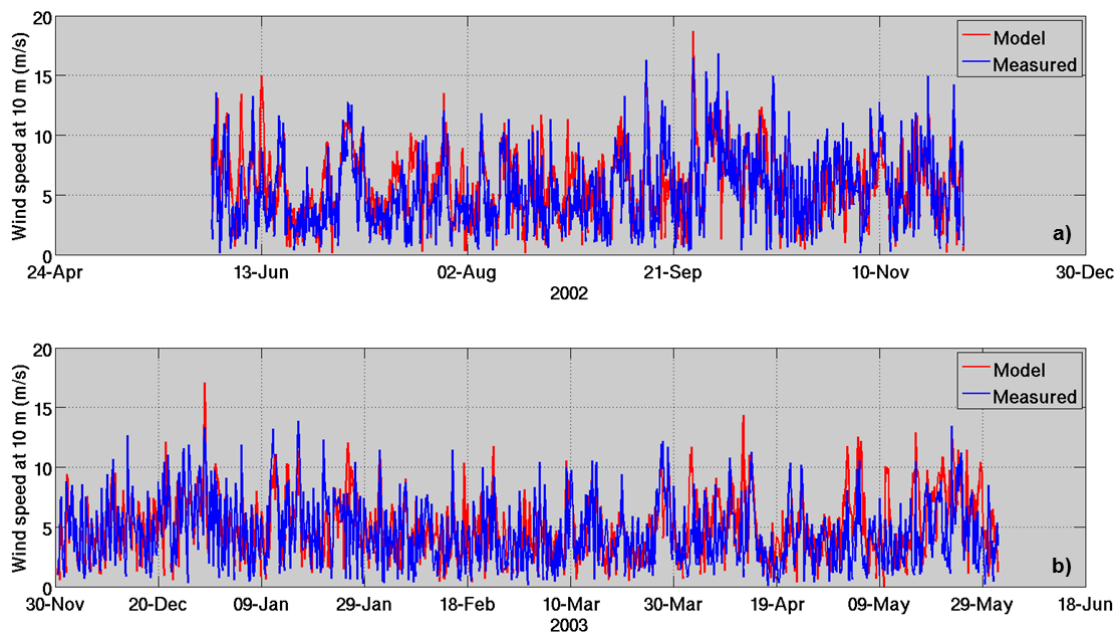


Figure 3.8 Measured and modelled wind speed at 10 m between (a) June and December 2002, and (b) January and June 2003.

Table 3.1 Comparison of measured and hindcast wind data. Accuracy measures for wind speed at Gisborne Airport between 2000 and 2008.

Statistics	Wind speed (m.s ⁻¹)
MAE	2.24
RMSE	2.85
MRAE	0.93
Bias	0.75
Scatter Index	0.6

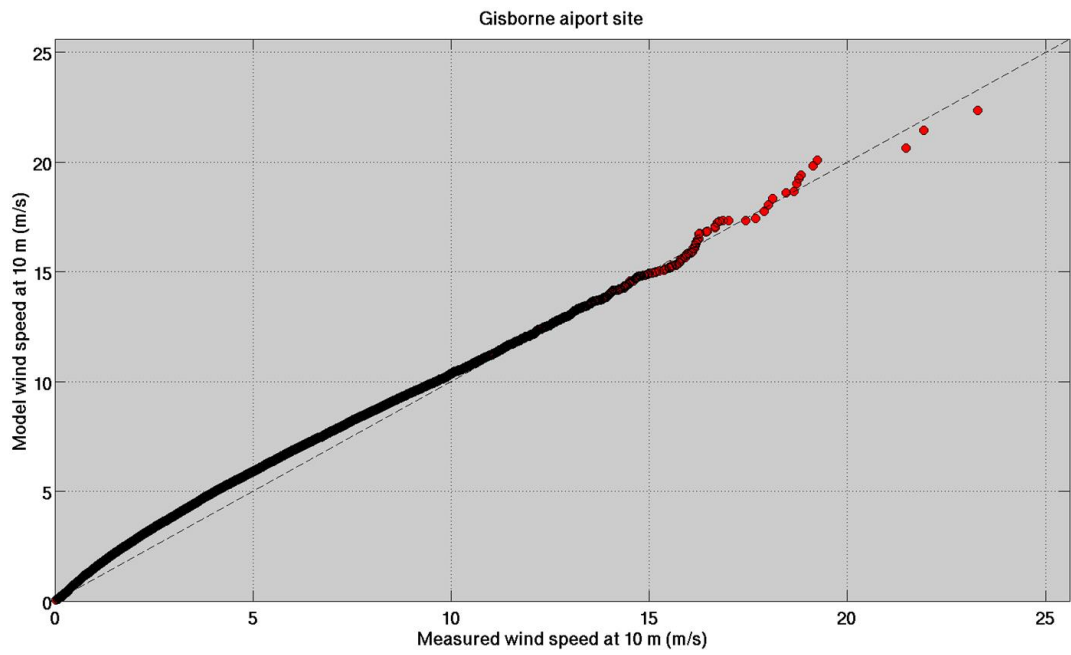


Figure 3.9 Quantile-Quantile plot of the 10 m measured and model wind speeds at Gisborne Airport for the period 2000 – 2008.

Gisborne Airport [177.9860 E; 38.6610 S]

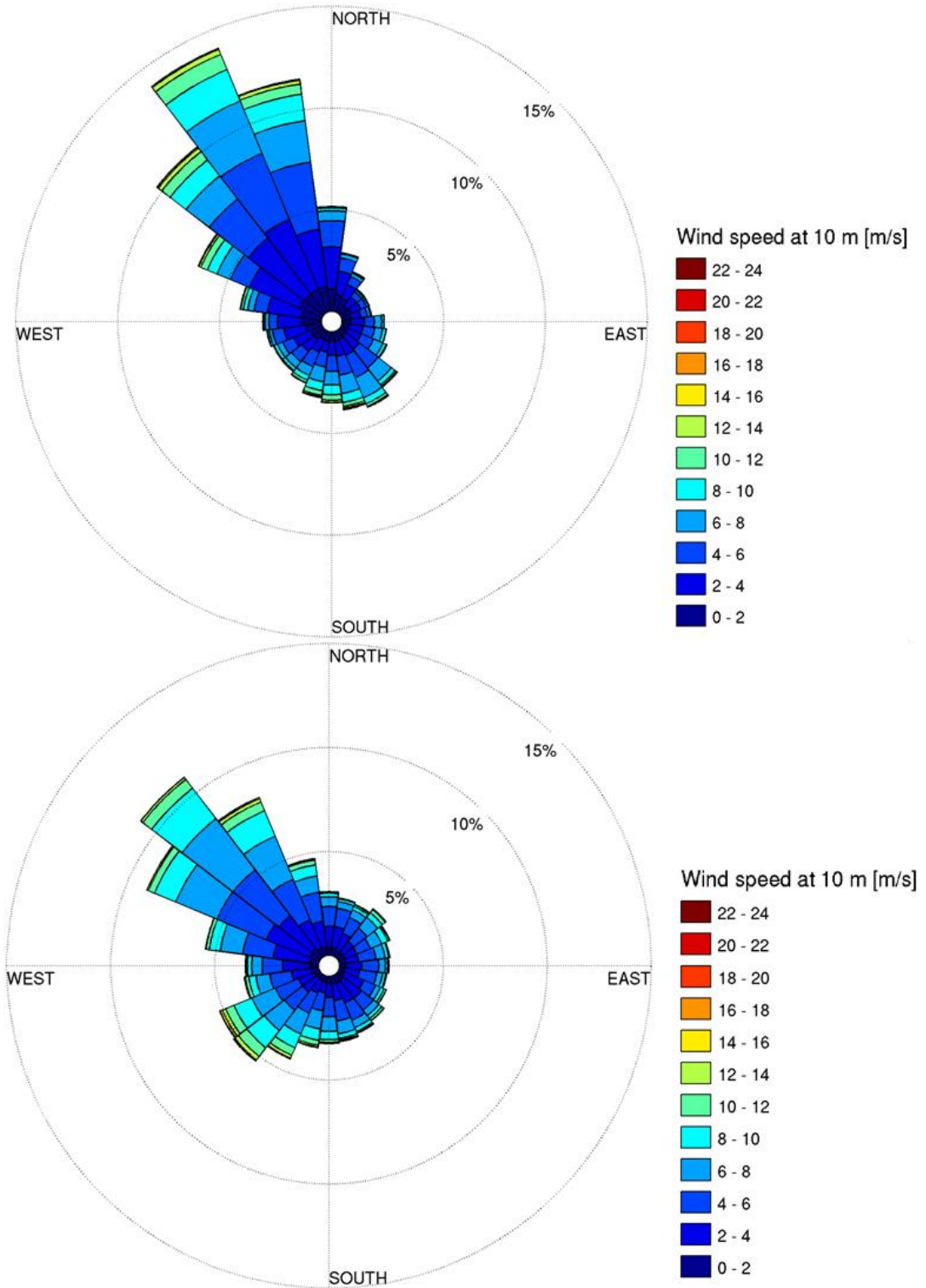


Figure 3.10 Measured (top) and model (bottom) wind roses at Gisborne Airport for the period 2000 – 2008. Winds are reported in the “coming from” directional reference.

3.2.2. ROMS water elevation and current velocities

The performance of the ROMS model was evaluated on the basis of water elevation and current time series recorded at five sites within Poverty Bay and on the adjacent shelf margin. Available measured data spanned periods in years 1996, 1998 and 2010. Results are presented in Figure 3.11 to Figure 3.22 and in Table 3.2.

Comparisons between measured and hindcast current velocities and water elevation at sites DW and NT indicate that the model predicts the continental shelf current variability well. The 2nd ADCP deployment at position NT showed particularly good correlations between model and observations. At site DW, water elevation and current velocities at 11 m (seabed) were well replicated. This suggests that the model adequately replicates the southward / northward shelf flowing currents. However, differences were observed between measured and hindcast data for the U-component of the current velocity near the seabed. The modelled U-velocity exhibited marked negative peaks up to -0.21 m.s^{-1} during the observational period, corresponding to relatively strong westward flows. These extreme events were not observed in the S4 current meter records.

Within Poverty Bay, the ROMS model showed good results for Site CM2 near Eastland Port. However, the resolution of the grid clearly limited the ability of the model to replicate the variability of the hydrodynamics controlled by river discharge and winds. This is particularly evident at position CM6 where the modelled near-bottom current velocities poorly agree with S4 current meter records.

Table 3.2 Comparison between measured and ROMS hindcast hydrodynamic data. Accuracy measures for current speed and water elevation at several sites over Poverty Bay and the adjacent shelf margin.

Sites	Parameters	Level	MAE	RMSE	MRAE	Bias	Scatter Index	Number of data
DW	Current speed	11 m	0.06	0.08	1.18	0.00	0.89	1028.00
	Current speed	31 m	0.05	0.07	1.11	0.00	0.94	1315.00
	Water elevation	/	0.12	0.14	1.20	0.03	/	1028.00
NT - Deployment 2	Current speed	18 m	0.07	0.09	0.69	-0.03	0.58	2308.00
	Current speed	35 m	0.06	0.08	0.71	-0.02	0.58	2308.00
NT - Deployment 3	Current speed	18 m	0.06	0.08	0.82	-0.02	0.65	2308.00
	Current speed	35 m	0.06	0.08	0.82	-0.02	0.65	2308.00
DT - Deployment 3	Current speed	35 m	0.06	0.08	0.72	-0.02	0.62	2308.00
	Current speed	69 m	0.06	0.08	0.76	-0.02	0.66	2308.00
CM2 - Deployment 2	Current speed	10 m	0.02	0.02	0.84	-0.00	0.90	284.00
	Water elevation	/	0.09	0.11	0.44	-0.05	/	285.00
CM6	Current speed	13 m	0.03	0.04	1.07	-0.01	0.78	336.00

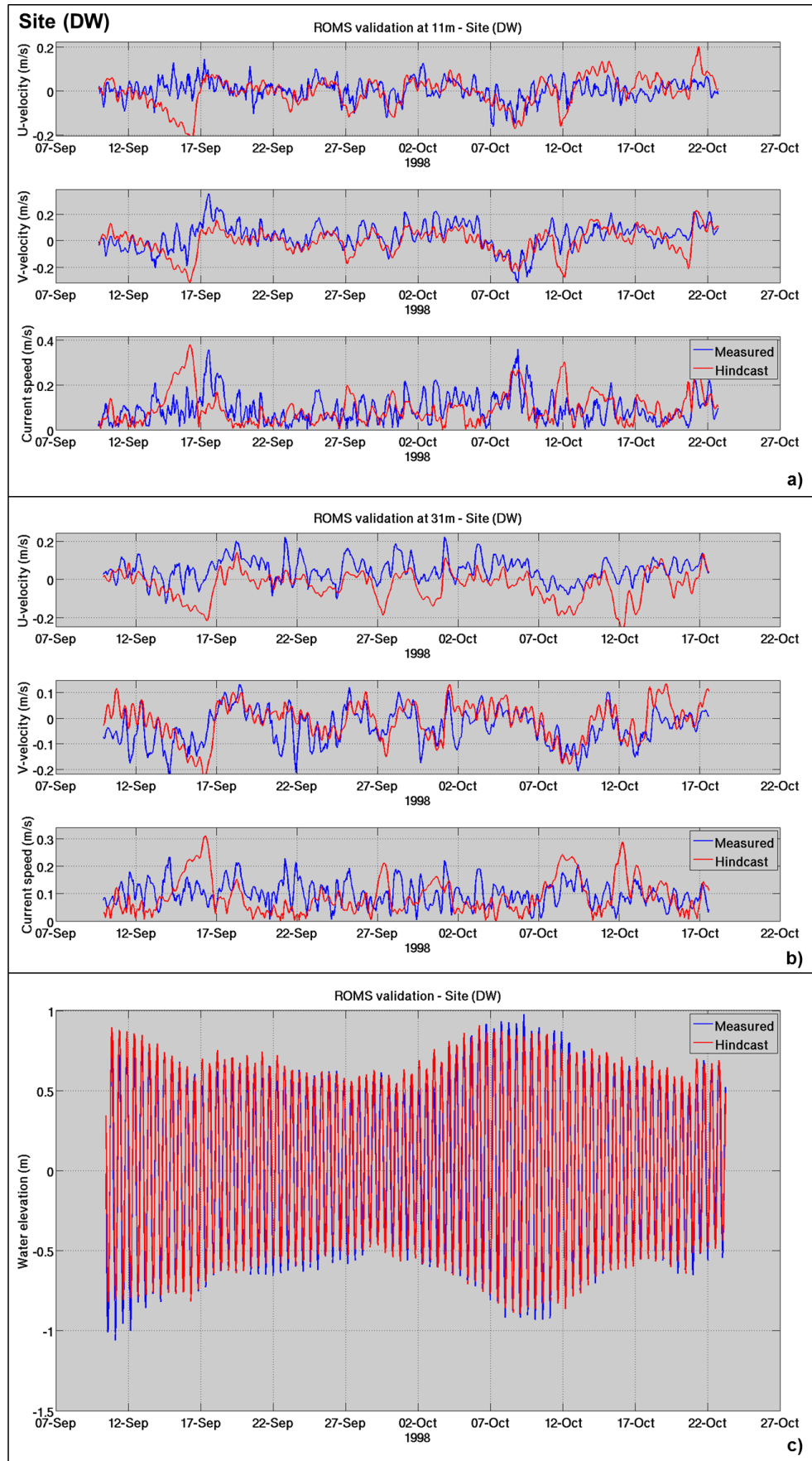


Figure 3.11 Comparison between measured and ROMS hindcast current and water elevation (c) time series at site DW at 11 m (a) and 31 m (b) (below sea level).

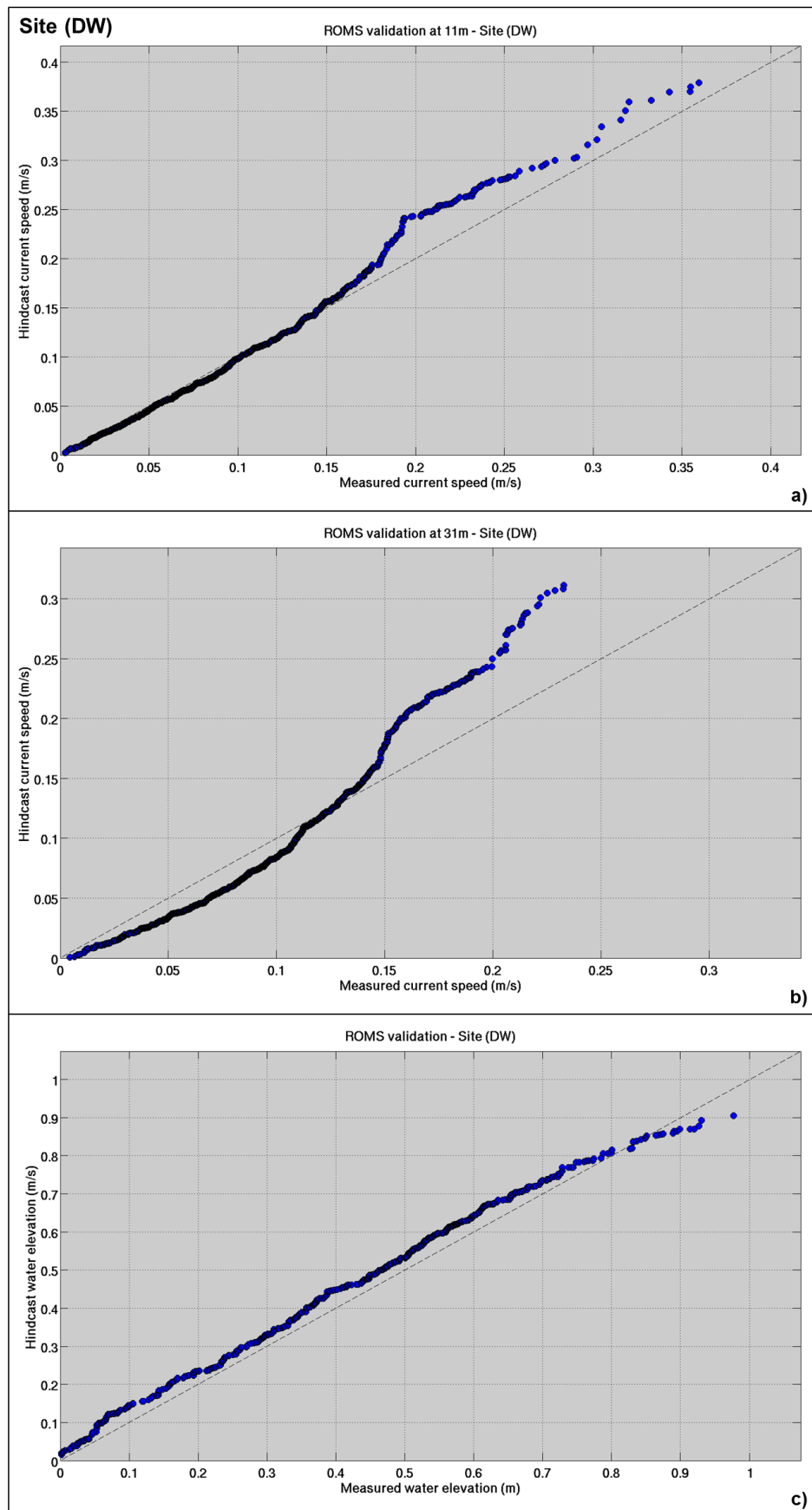


Figure 3.12 Quantile-Quantile plots created from measured and ROMS hindcast current and water elevation (c) time series at site DW at 11 m (a) and 31 m (b) (below sea level). The dashed black line indicates a perfect agreement between the distributions.

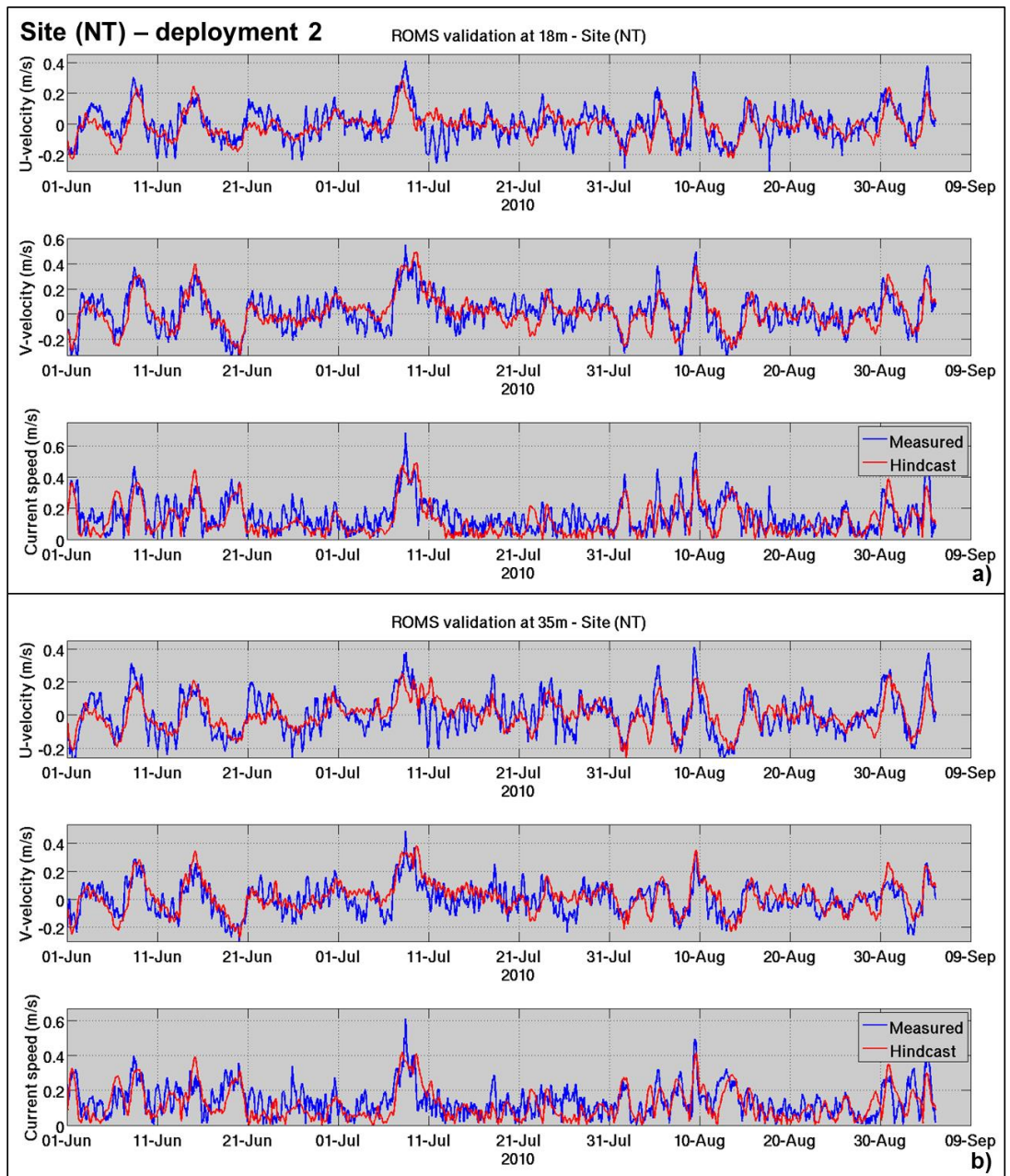


Figure 3.13 Comparison between measured and ROMS hindcast current time series at site NT at 18 m (a) and 35 m (b) (below sea level) for the second deployment.

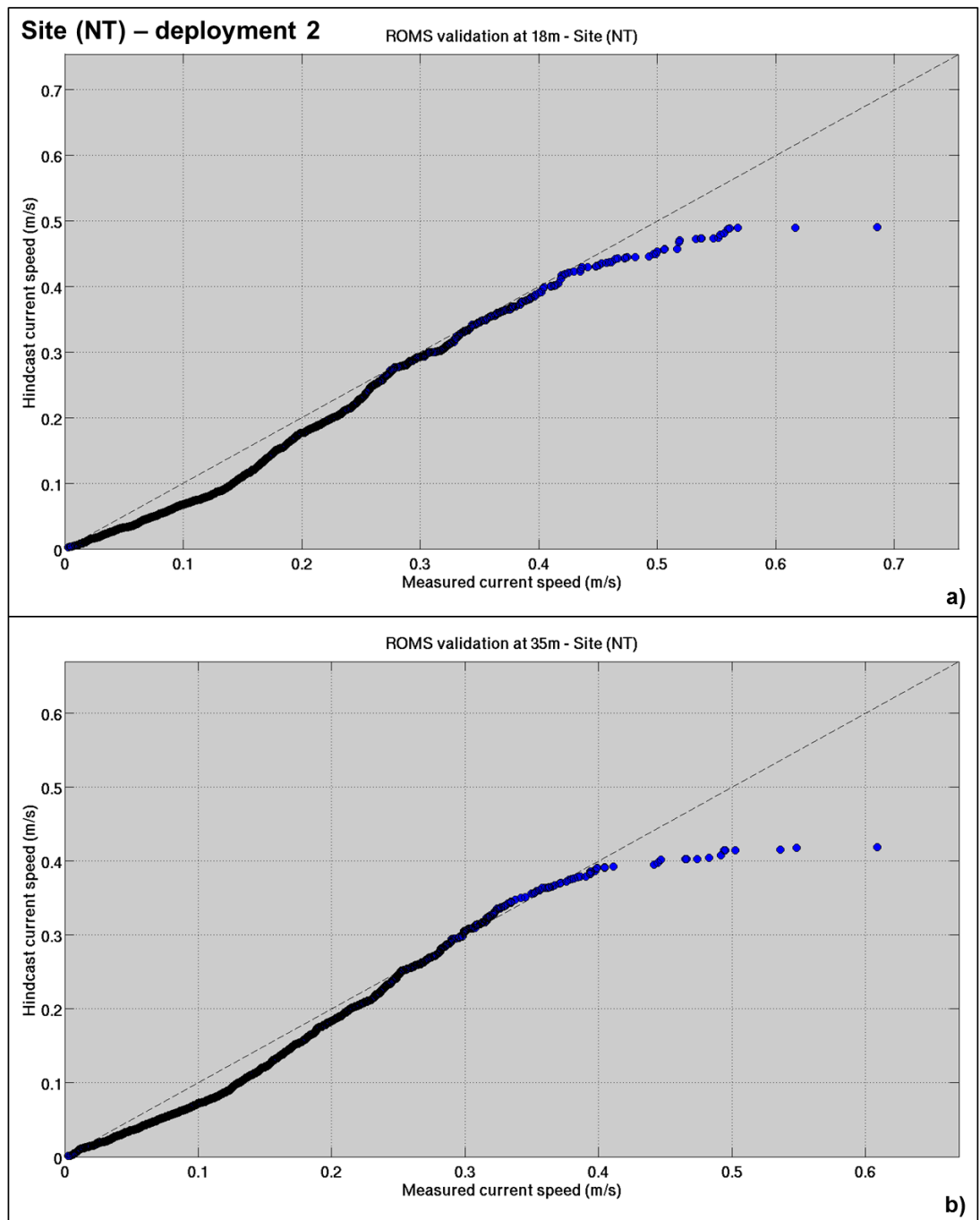


Figure 3.14 Quantile-Quantile plots created from measured and ROMS hindcast current time series at site N) at 18 m (a) and 35 m (b) (below sea level) for the second deployment. The dashed black line indicates a perfect agreement between the distributions.

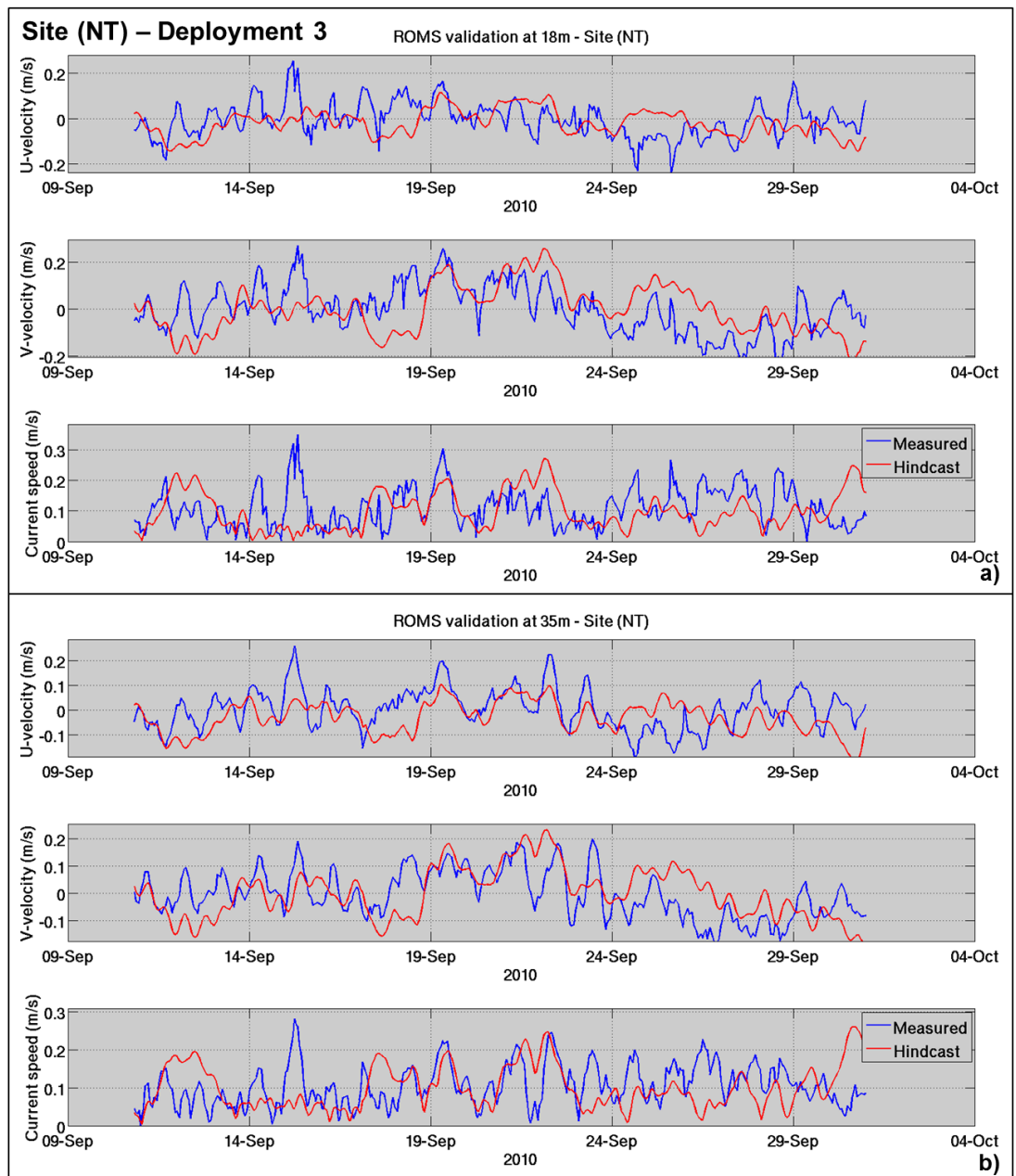


Figure 3.15 Comparison between measured and ROMS hindcast current time series at site N) at 18 m (a) and 35 m (b) (below sea level) for the third deployment.

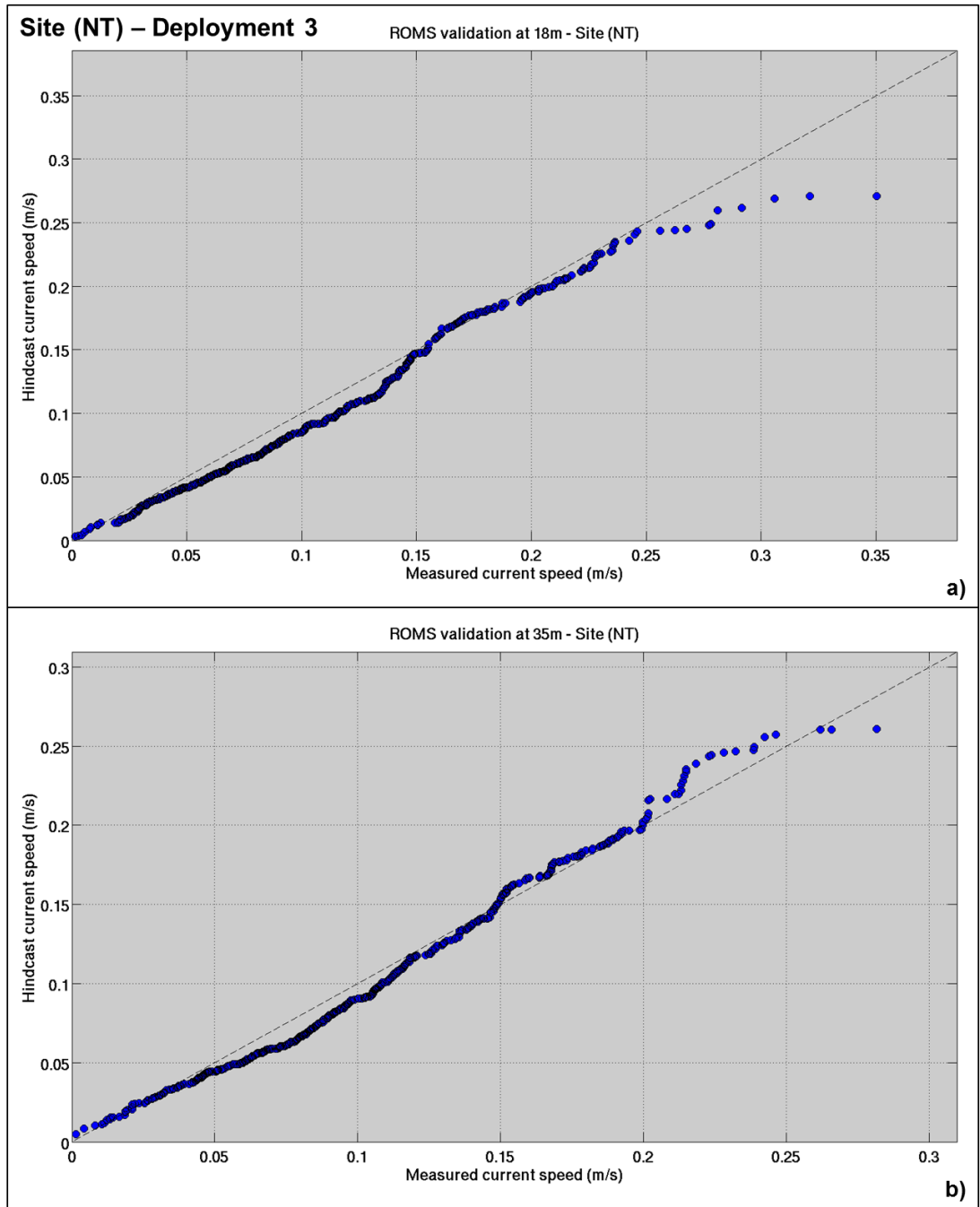


Figure 3.16 Quantile-Quantile plots created from measured and ROMS hindcast current time series at siteNT at 18 m (a) and 35 m (b) (below sea level) for the third deployment. The dashed black line indicates a perfect agreement between the distributions.

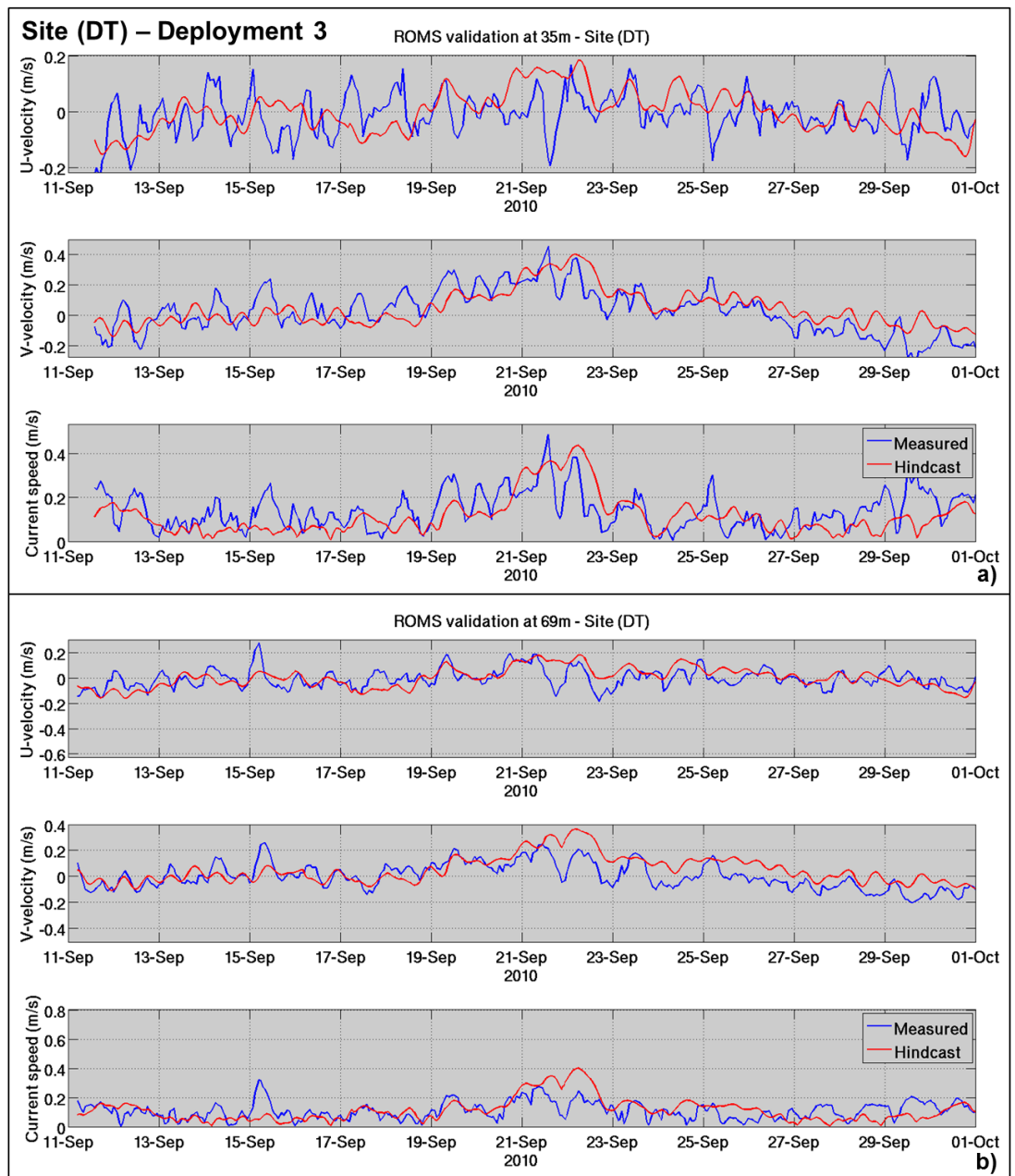


Figure 3.17 Comparison between measured and ROMS hindcast current time series at site DT at 35 m (a) and 69 m (b) (below sea level) for the third deployment.

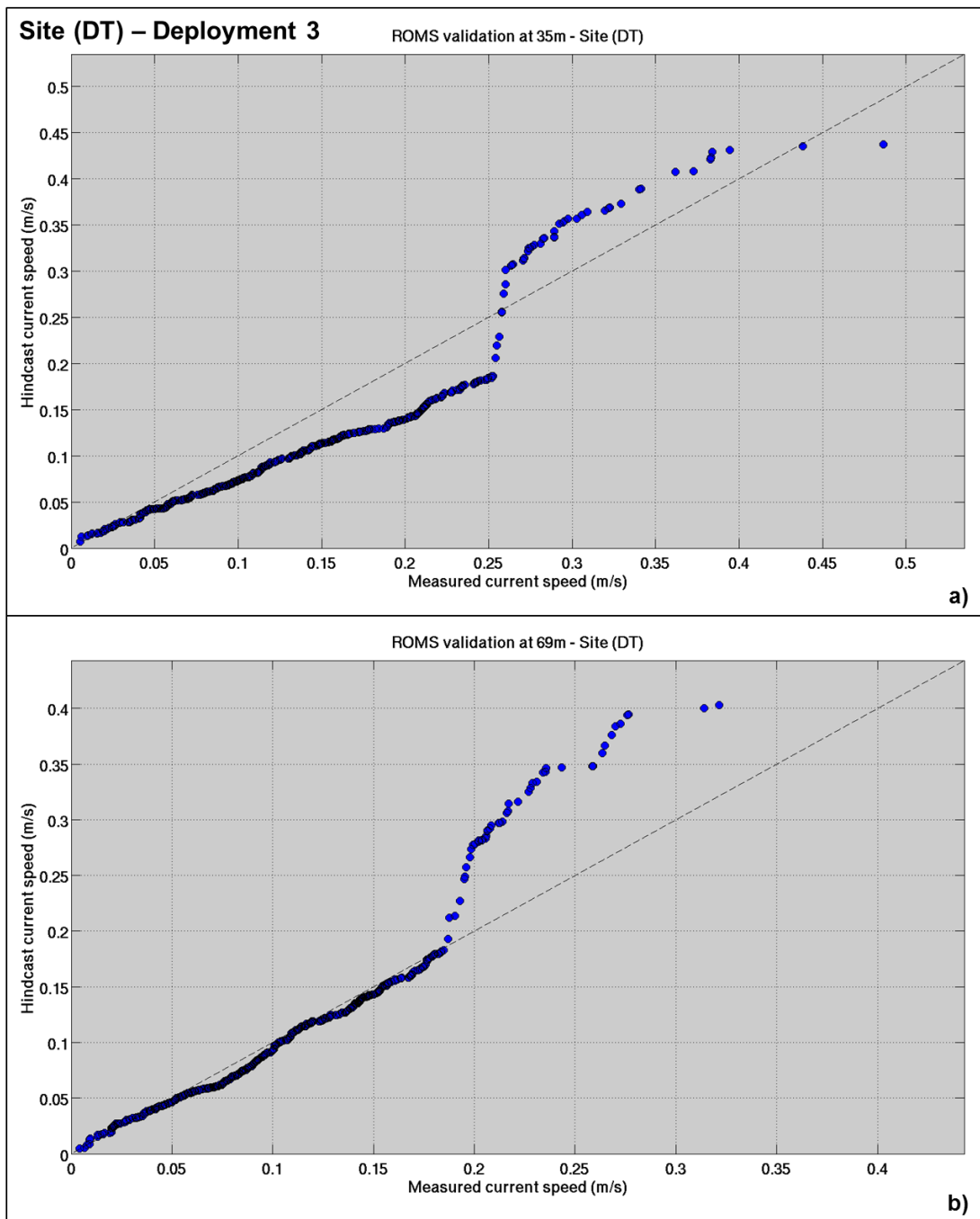


Figure 3.18 Quantile-Quantile plots created from measured and ROMS hindcast current time series at site DT at 35 m (a) and 69 m (b) (below sea level) for the third deployment. The dashed black line indicates a perfect agreement between the distributions.

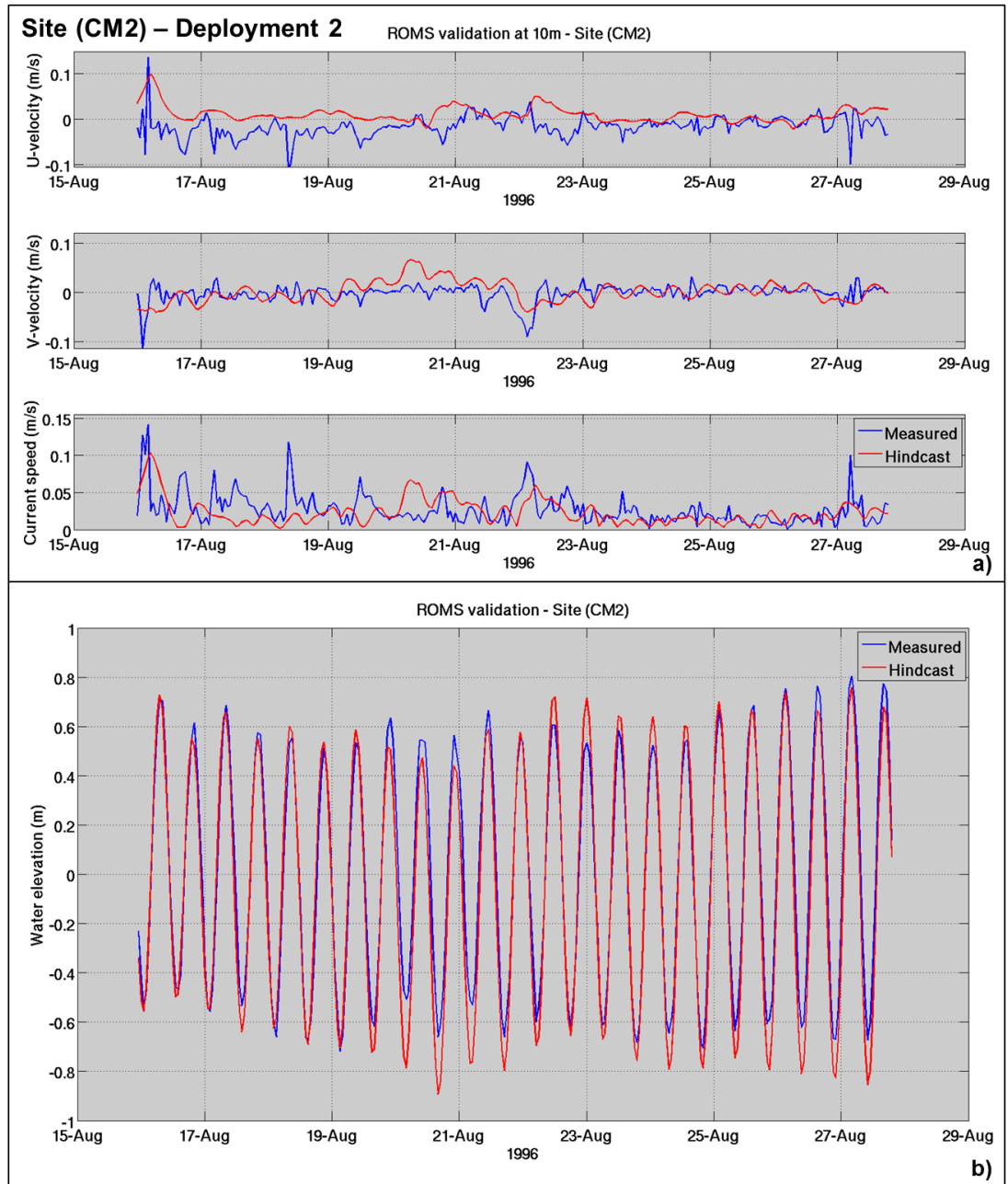


Figure 3.19 Comparison between measured and ROMS hindcast current (a) and water elevation (b) time series at site CM2 at 10 m (below sea level) for the second deployment.

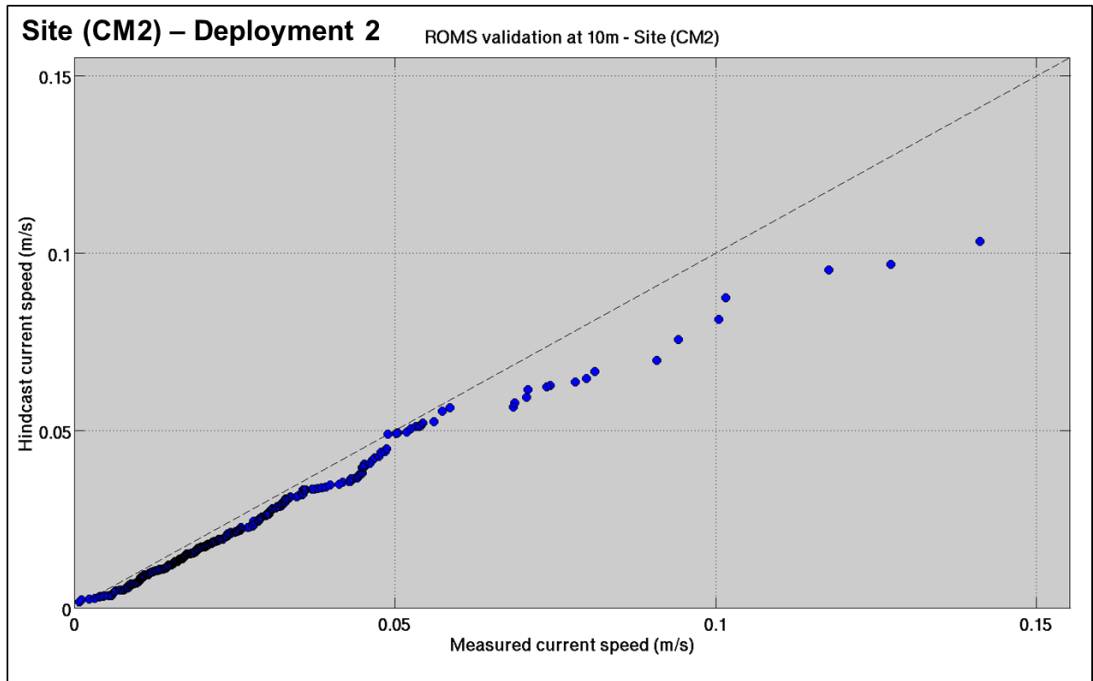


Figure 3.20 Quantile-Quantile plot created from measured and ROMS hindcast current time series at site CM2 at 10 m (below sea level) for the second deployment. The dashed black line indicates a perfect agreement between the distributions.

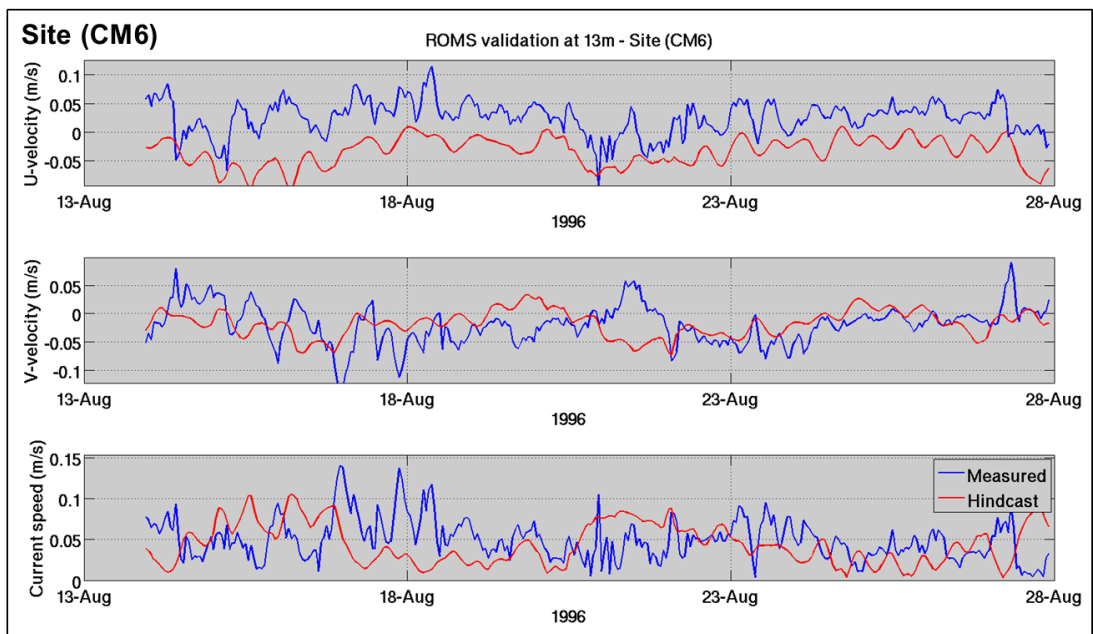


Figure 3.21 Comparison between measured and ROMS hindcast current time series at site CM6 at 13 m (below sea level).

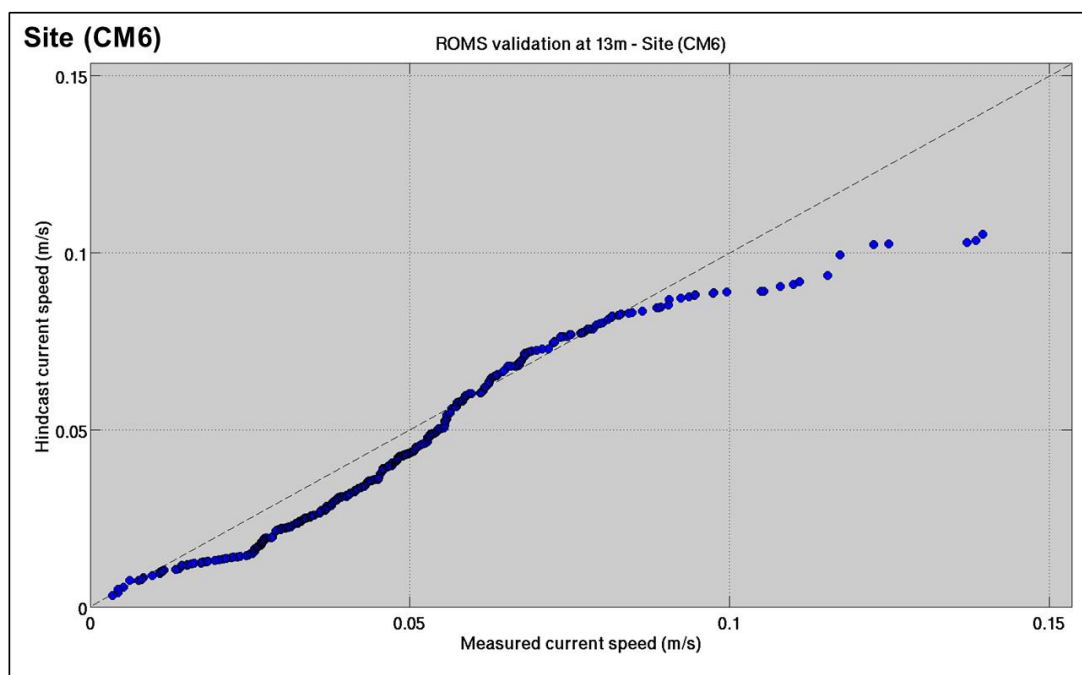


Figure 3.22 Quantile-Quantile plot created from measured and ROMS hindcast current time series at site CM6 at 13 m (below sea level). The dashed black line indicates a perfect agreement between the distributions.

3.2.1. SCHISM water elevation and current velocities

Comparisons between observations and SCHISM model data at positions CM2 and CM3 are presented in Figure 3.23 to Figure 3.26, while summary statistics are given in Table 3.3. Results highlighted a significant improvement of the modelling performance in SCHISM compared to the PB-ROMS nest. The water elevation time series produced by SCHISM was coherent with the records at CM2. Although some of the moderate flow events were not fully captured in SCHISM, the distribution of both measured and model current velocities were relatively close. This is an important feature, as the morphological and plume model strategies are more dependent on the statistical distribution of velocities than on the good correlation between model and field records within the time-domain. More broadly, this model skill assessment indicated that the SCHISM model of Poverty Bay is suitable for providing hydrodynamic conditions to subsequent plume and morphological models.

Table 3.3 Comparison between measured and SCHISM hindcast hydrodynamic data. Accuracy measures for current speed at two sites within Poverty Bay.

Sites	Parameters	Level	MAE	RMSE	MRAE	Bias	Scatter Index	Number of data
CM2	Current speed	10 m	0.0174	0.0239	0.8615	0.0007	0.8893	1153
CM6	Current speed	13 m	0.0299	0.396	0.7952	-0.0026	0.7929	961

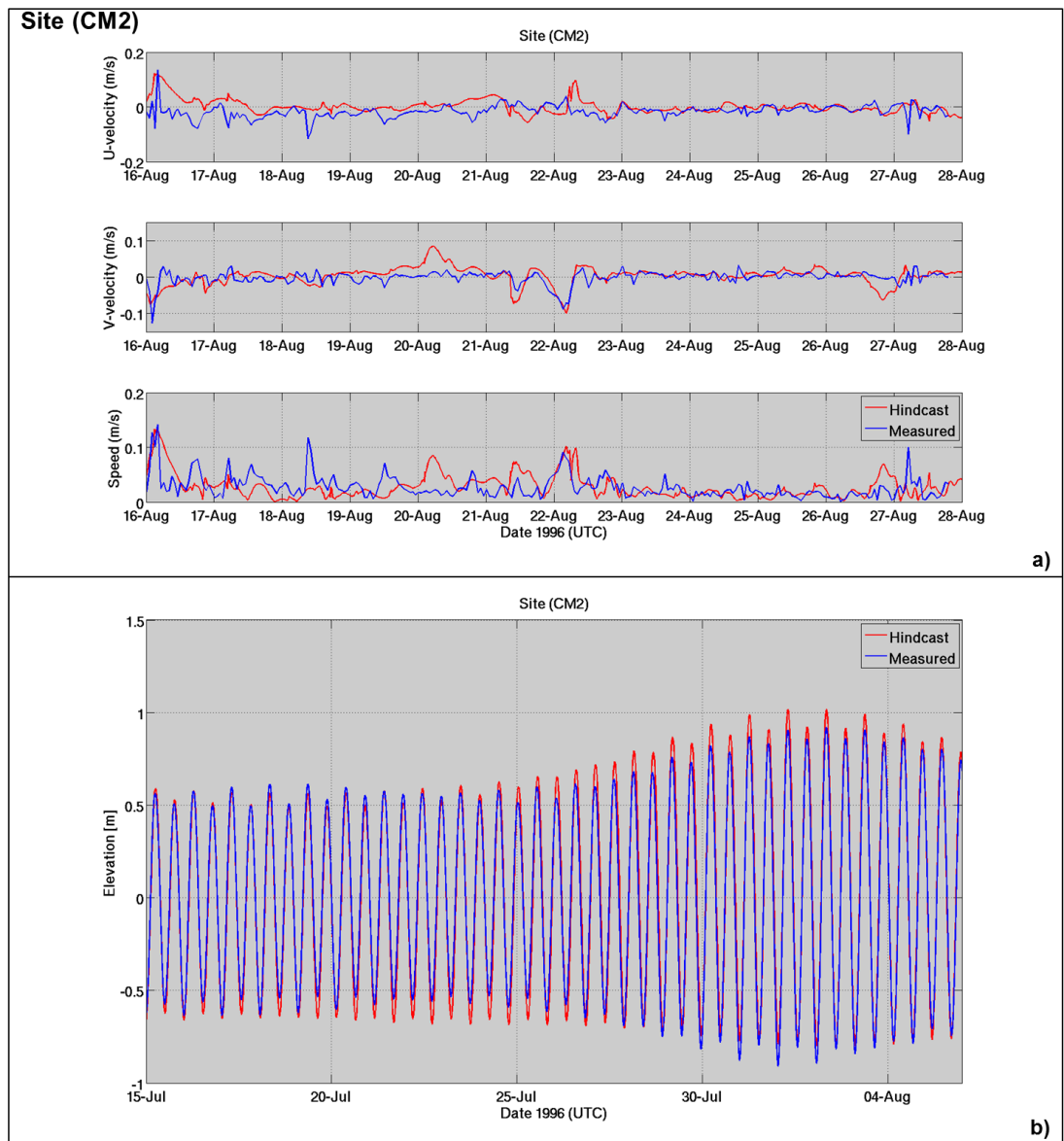


Figure 3.23 Comparison between measured and SCHISM hindcast current (a) and water elevation (b) time series at site CM2 at 10 m (below sea level) for the first and second deployment, respectively.

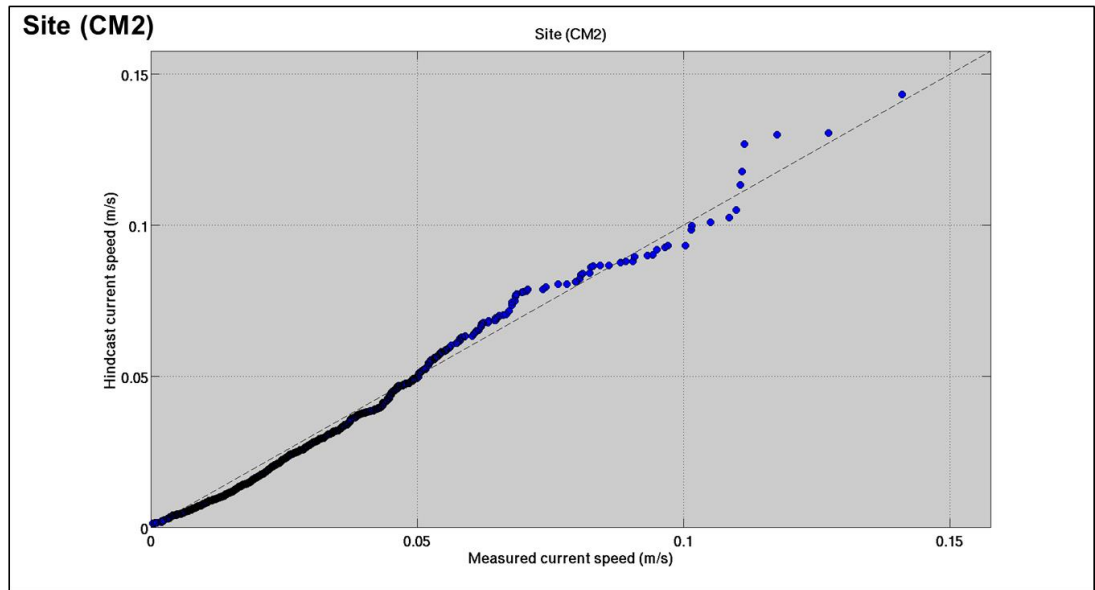


Figure 3.24 Quantile-Quantile plot created from measured and SCHISM hindcast current time series at site CM2 at 10 m (below sea level). The dashed black line indicates a perfect agreement between the distributions.

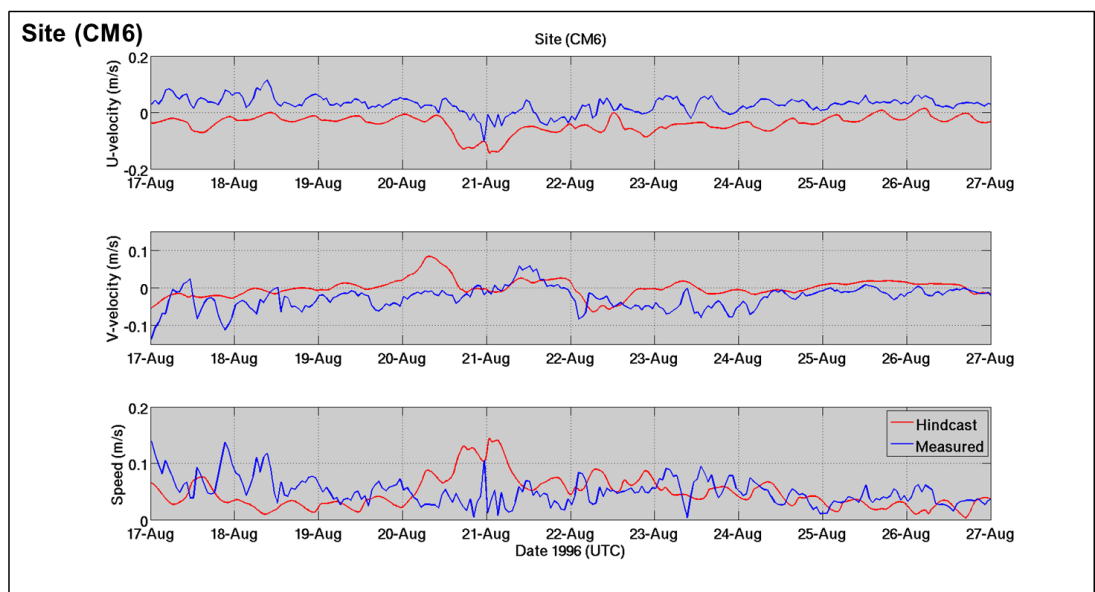


Figure 3.25 Comparison between measured and SCHISM hindcast current time series at site CM6 at 13 m (below sea level).

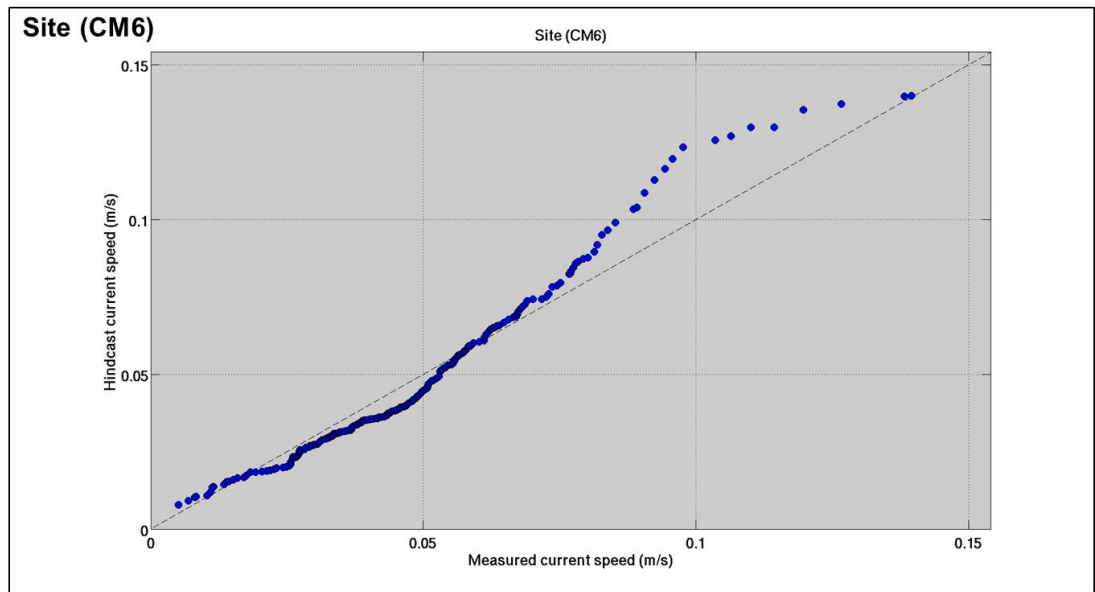


Figure 3.26 Quantile-Quantile plot created from measured and SCHISM hindcast current time series at site CM6 at 13 m (below sea level). The dashed black line indicates a perfect agreement between the distributions.

4. SUMMARY

Ocean currents were simulated with two different models to investigate both regional and local scales. The open-source ROMS model was used to perform 3D hydrodynamic downscaling of the oceanic and tidal flows over the continental shelf adjacent to Poverty Bay.

Qualitative and quantitative validation of ROMS with literature and measured data showed that the model adequately represented the governing hydrodynamics over the continental shelf margin and at the entrance to Poverty Bay. By contrast, results at nearshore sites within Poverty Bay suggested that the model resolution was not adequate for fully replicating the complex hydrodynamics in the bay.

The implementation of the unstructured FE SCHISM model nested within the PB-ROMS domain provided significant improvements in the nearshore predictive capability of the numerical models. Although some moderate flow events were not fully captured by the model, the overall statistical distribution of current velocities was satisfactory at the Waipaoa river mouth and near Eastland Port. In this context, the SCHISM model is considered suitable for forcing the subsequent morphological and plume models as part of the dredging and disposal impact assessments.

5. REFERENCES

- Becker, J.J., Sandwell, D.T., Smith, W.H.F., Braud, J., Binder, B., Depner, J., Fabre, D., Factor, J., Ingalls, S., Kim, S.H., others, 2009. Global bathymetry and elevation data at 30 arc seconds resolution: SRTM30_PLUS. *Mar. Geod.* 32, 355–371.
- Beckman, A., and Haidvogel, D., 1993. Numerical simulation of flow around a tall isolated seamount. *J Phys Ocean.* 23, 1736–1753.
- Bever, A.J., 2010. Integrating space-and time-scales of sediment-transport for Poverty Bay, New Zealand. The College of William and Mary.
- Black, K.P., Gorman, R.G., Stephens, S.A., Beamsley, B.J., Healy, T.R., Bell, R.G., Oldman, J.W., 1997. Numerical Modelling for the Port Gisborne Expansion, A report on behalf of Port Gisborne Ltd., Centre of Excellence in Coastal Oceanography and Marine Geology, incorporating the Coastal Marine Group, Department of Earth Sciences, The university of Waikato, and the National Institute of Water and Atmospheric Research, Hamilton.
- Egbert, G.D., Erofeeva, S.Y., 2002. Efficient inverse modeling of barotropic ocean tides. *J. Atmospheric Ocean. Technol.* 19, 183–204.
- Fairall, C. W., Bradley, E. F., Hare, J. E., Grachev, A. A., Edson, J. B., 2003. Bulk parameterization of air-sea fluxes: Updates and verification for the COARE algorithm. *J. Clim.* 16, 571–591.
- Haidvogel, D.B, Arango, H.G., Budgell, W.P., Cornuelle, B.D., Curchitser, E., Di Lorenzo, E., Fennel, K., Geyer, W.R., Hermann, A.J., Lanerolle, L., Levin, J., McWilliams, J.C., Miller, A.J., Moore, A.M., Powell, T.M., Shchepetkin, A.F., Sherwood, C.R., Signell, R.P., Warner, J.C., Wilkin, J., 2008. Ocean forecasting in terrain-following coordinates: Formulation and skill assessment of the Regional Ocean Modeling System. *J. Comput. Phys.* 227, 3595–3624.
- Hale, R.P., Ogston, A.S., Walsh, J.P., Orpin, A.R., 2014. Sediment transport and event deposition on the Waipaoa River Shelf, New Zealand. *Cont. Shelf Res.* 86, 52–65.
- Mellor, G.L., 1998. Users guide for a three dimensional, primitive equation, numerical ocean model. Program in Atmospheric and Oceanic Sciences, Princeton University Princeton, NJ 08544-0710.
- Stephens, S.A., Bell, R.G., Black, K.P., 2001. Complex circulation in a coastal embayment: Shelf-current, wind and density-driven circulation in Poverty Bay, New Zealand. *J. Coast. Res.* 45–59.
- Zhang, Y.J., Ateljevich, E., Yu, H.-C., Wu, C.H., Jason, C.S., 2015. A new vertical coordinate system for a 3D unstructured-grid model. *Ocean Model.* 85, 16–31.
- Zhang, Y.L., Baptista, A.M., 2008. A semi-implicit Eulerian-Lagrangian finite element model for cross-scale ocean circulation. *Ocean Model.* 21, 71–96.

APPENDIX A. MEASURED AND HINDCAST WIND ROSES AT HICKS BAY

Hicks Bay [178.314 E; 37.564 S]

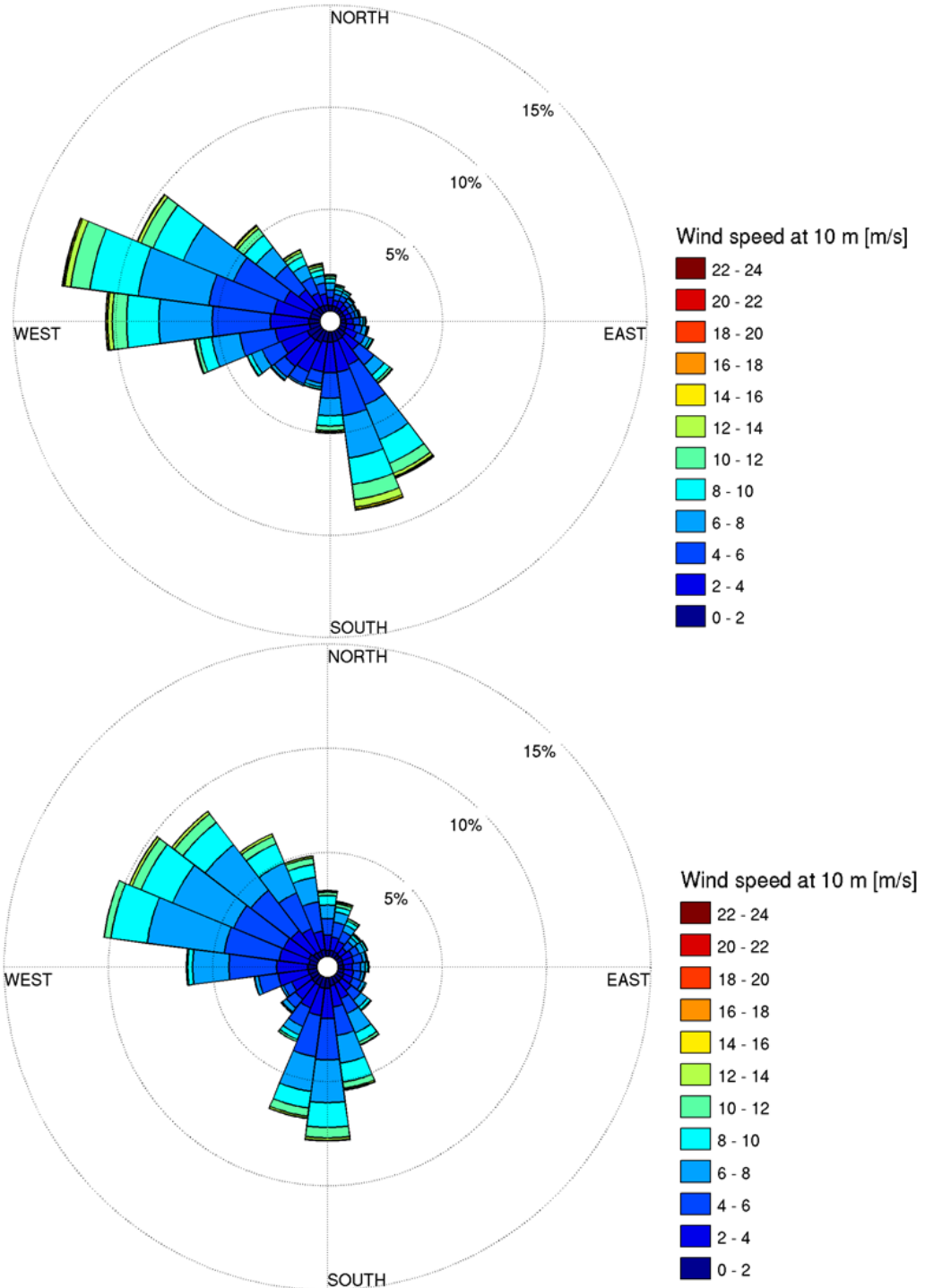


Figure A.1 Measured and hindcast wind rose at 10 m extracted at Hicks Bay between 2000 and 2008.

APPENDIX B. MONTHLY DEPTH-AVERAGED AND SURFACE CURRENT FIELDS

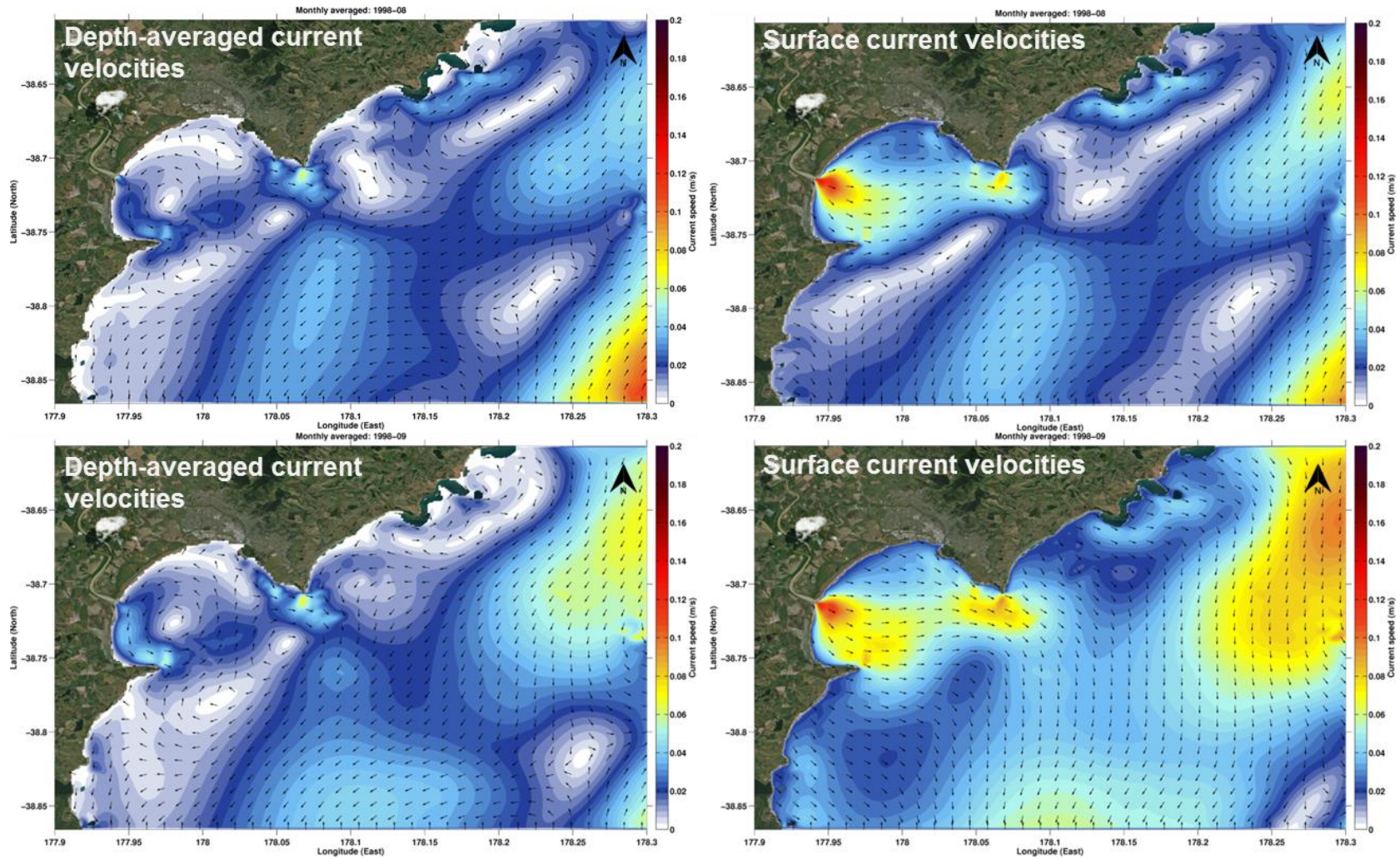


Figure B.1 Monthly depth-averaged and surface current velocities for August (left) and September 1998 (right) predicted by ROMS.

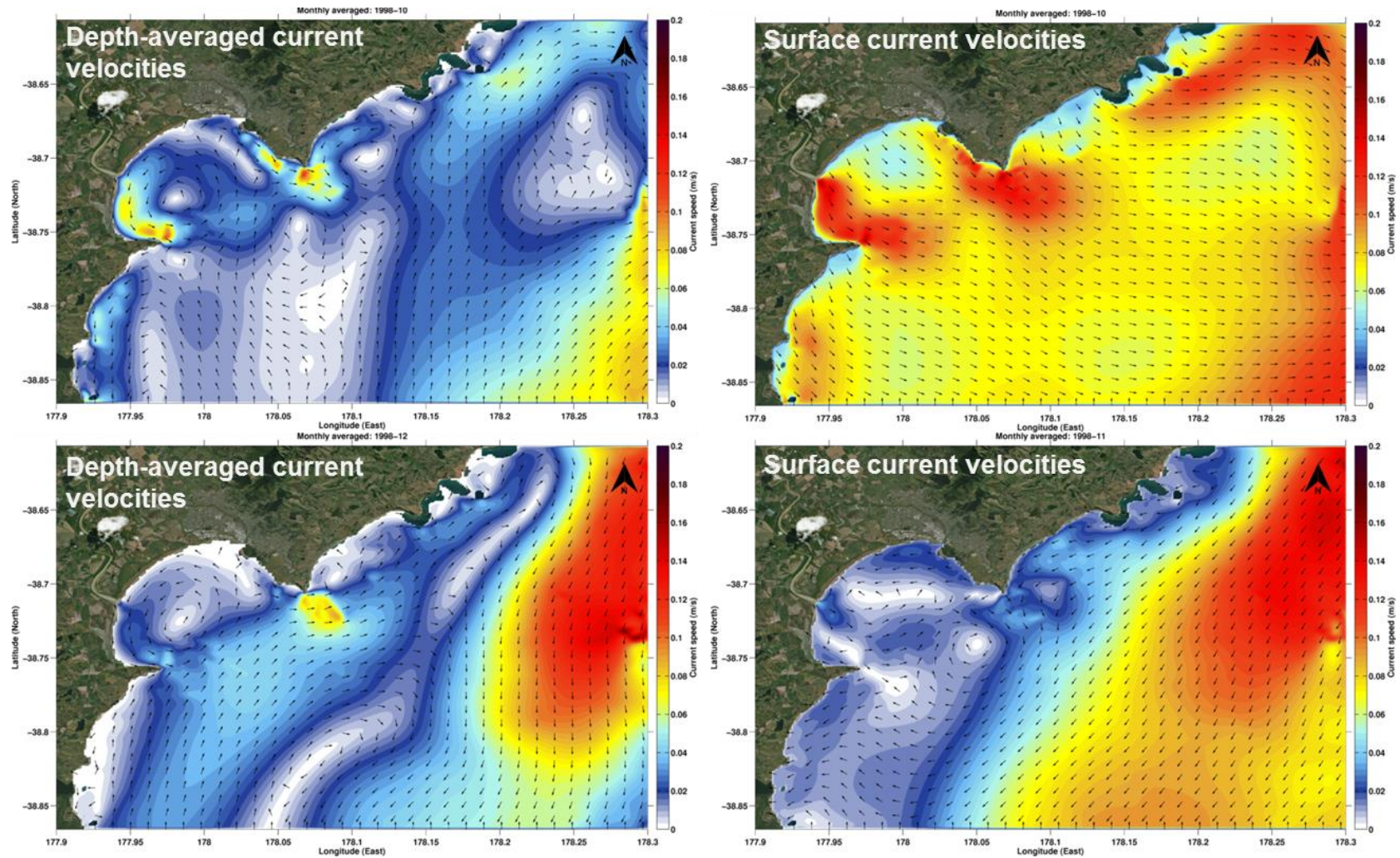


Figure B.2 Monthly depth-averaged and surface current velocities for October (left) and November 1998 (right) predicted by ROMS.

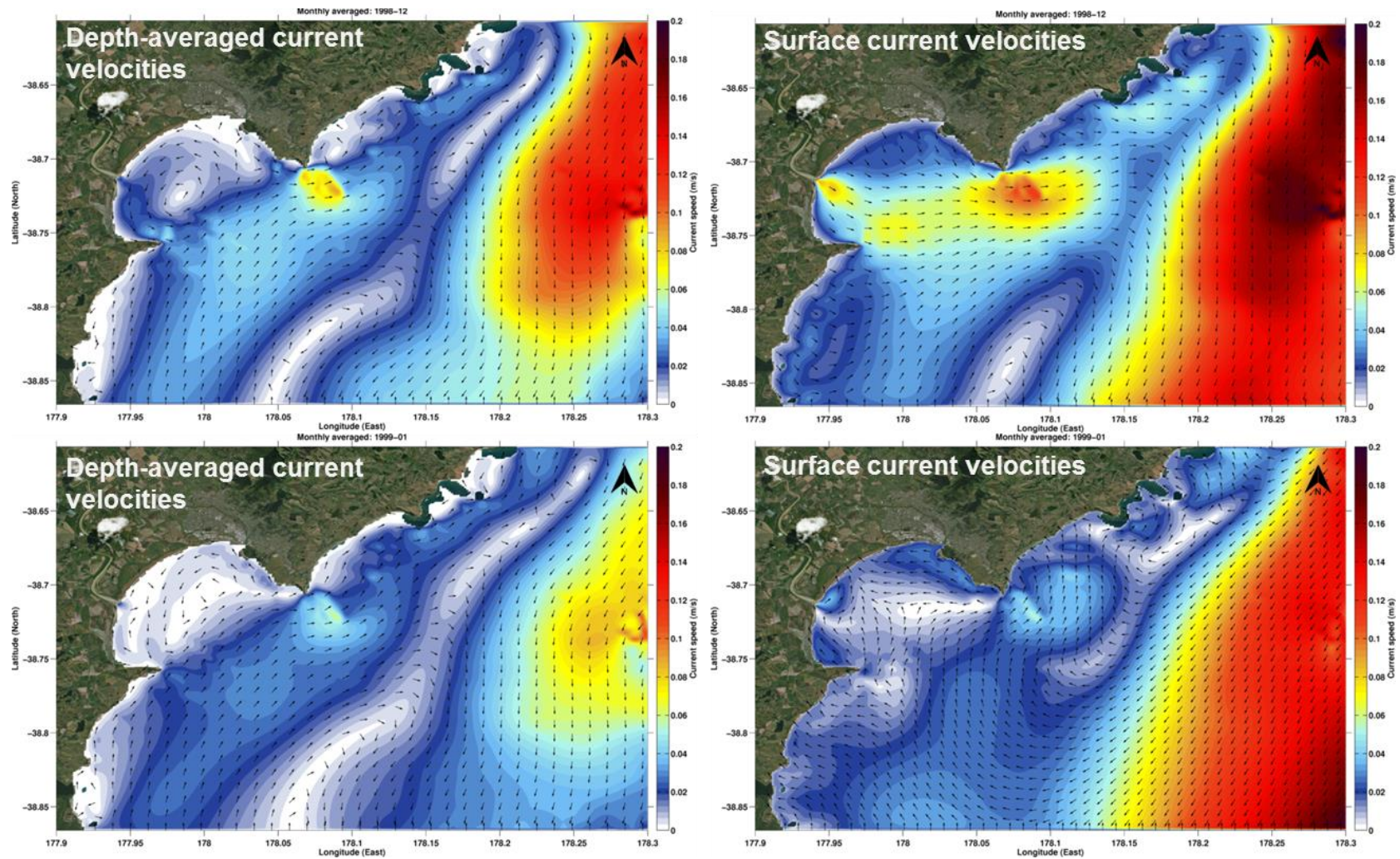


Figure B.3 Monthly depth-averaged and surface current velocities for December (left) and January 1998/99 (right) predicted by ROMS.

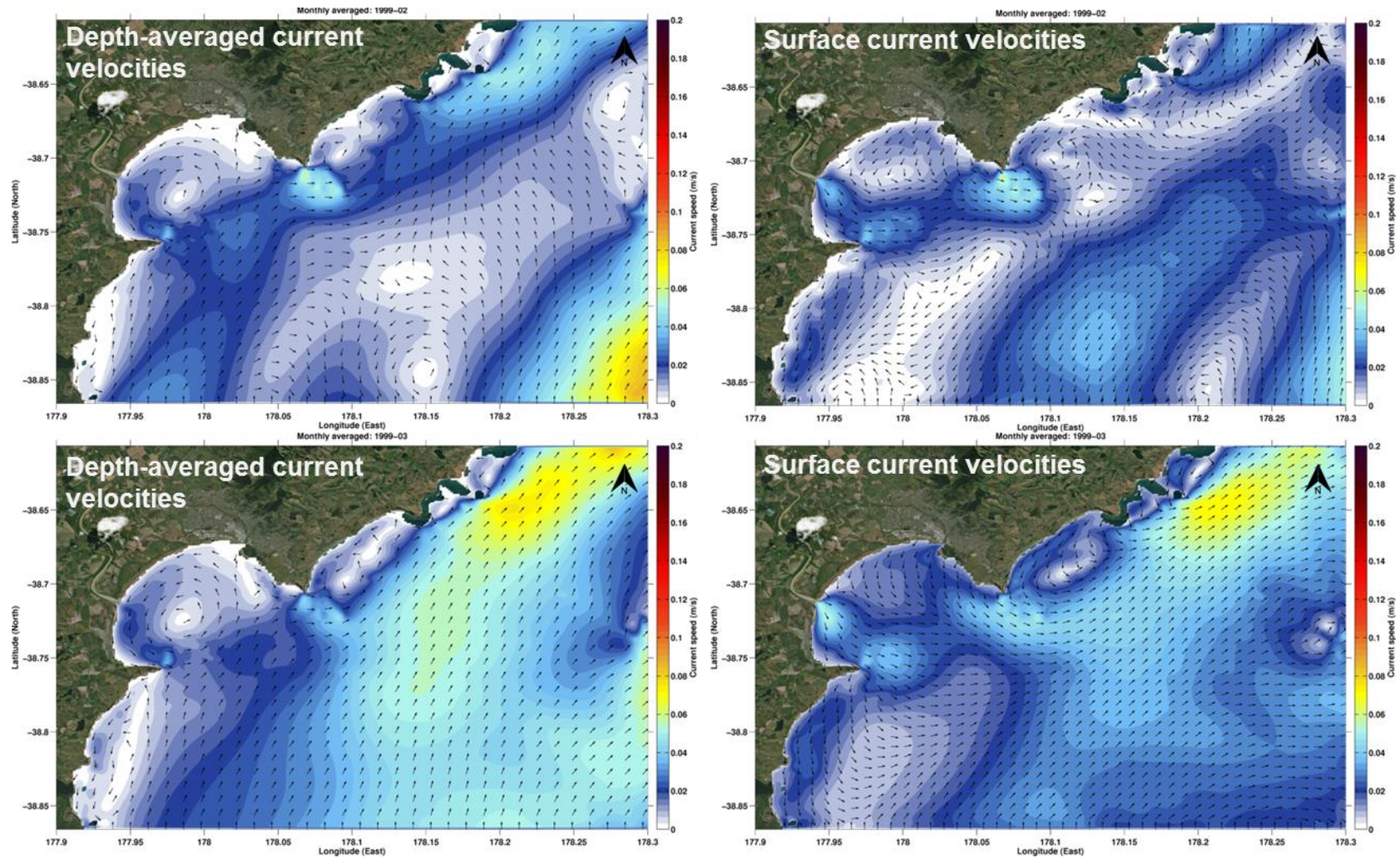


Figure B.4 Monthly depth-averaged and surface current velocities for February (left) and March 1999 (right) predicted by ROMS.

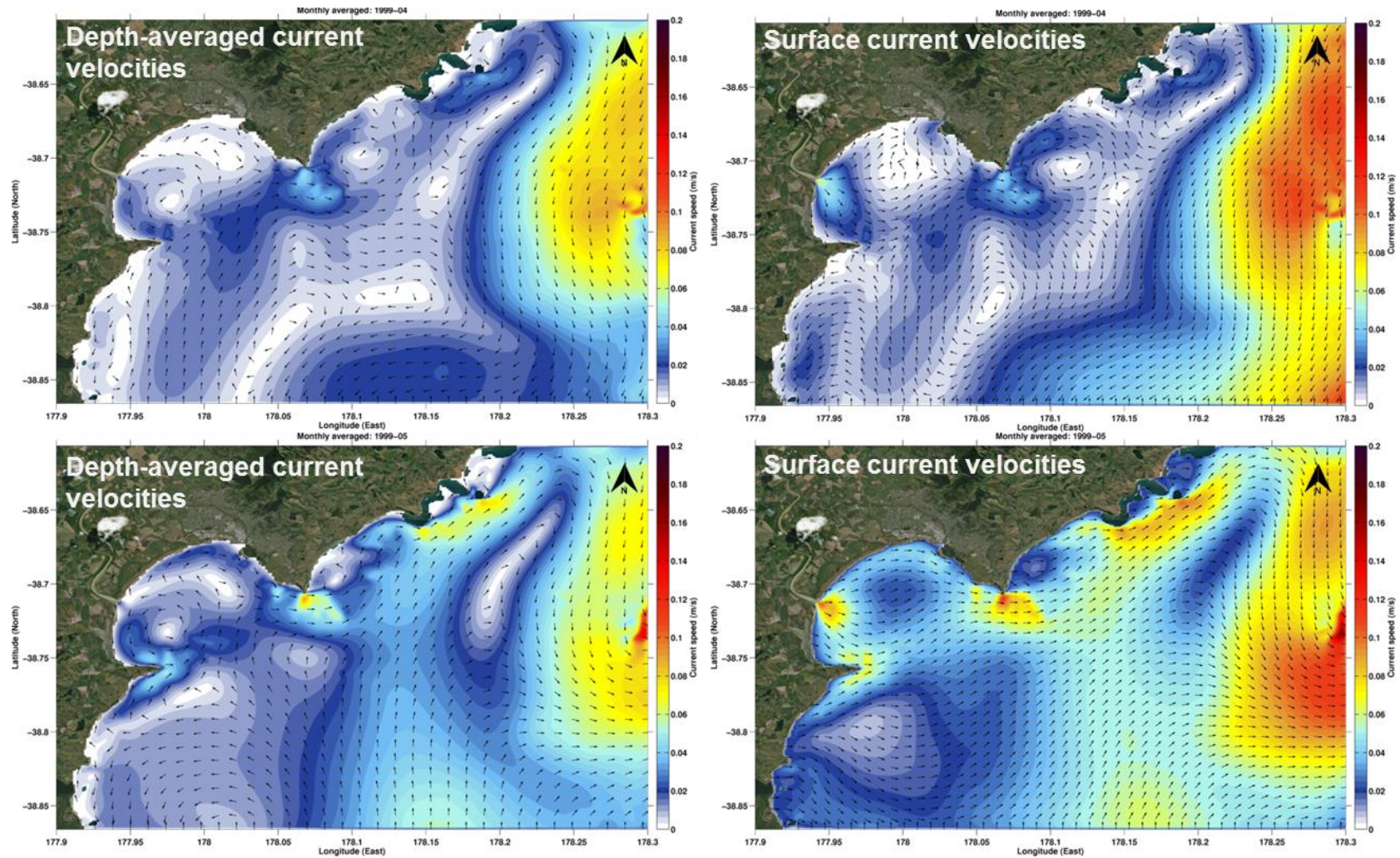


Figure B.5 Monthly depth-averaged and surface current velocities for April (left) and May 1999 (right) predicted by ROMS.

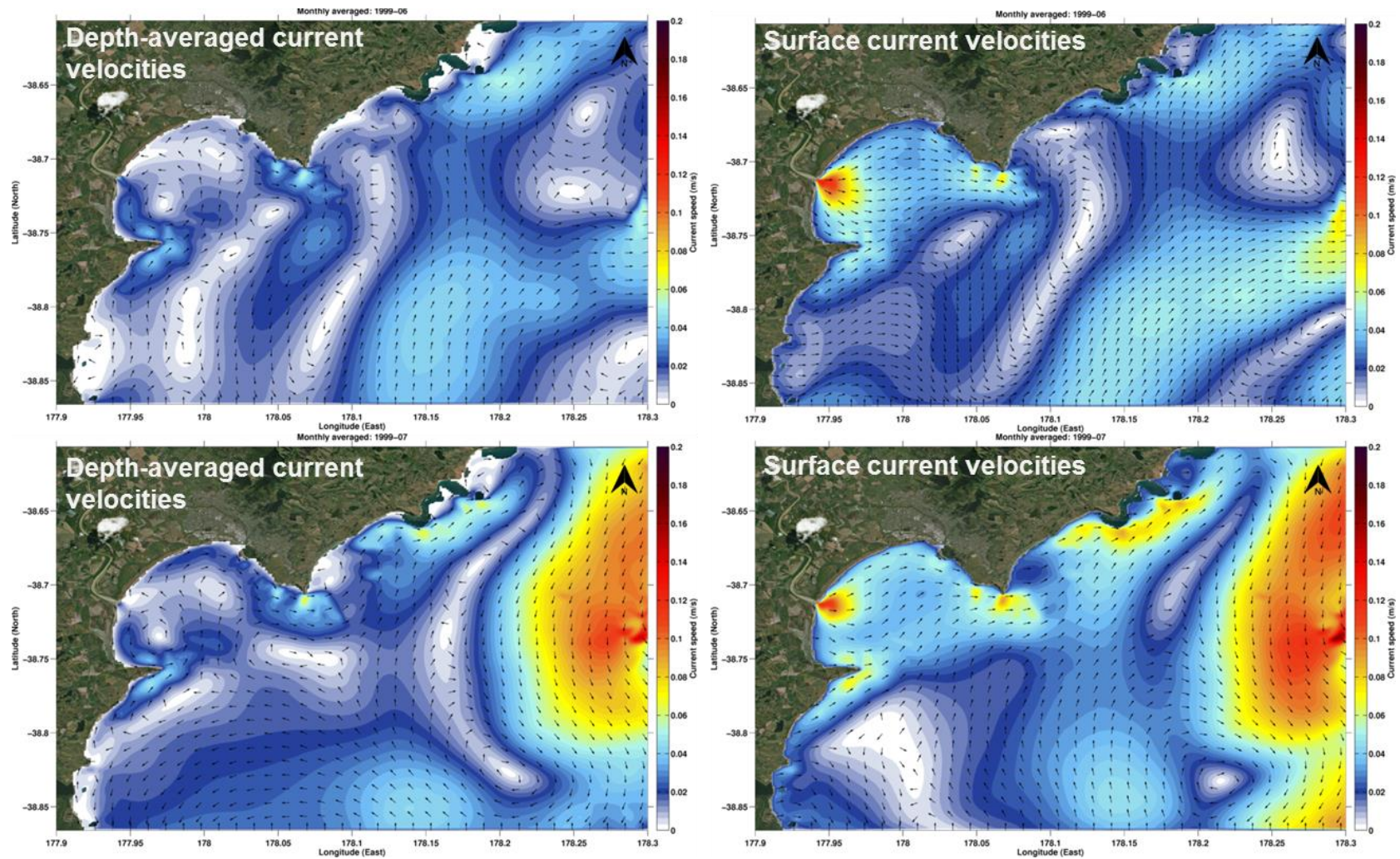


Figure B.6 Monthly depth-averaged and surface current velocities for June (left) and July 1999 (right) predicted by ROMS.